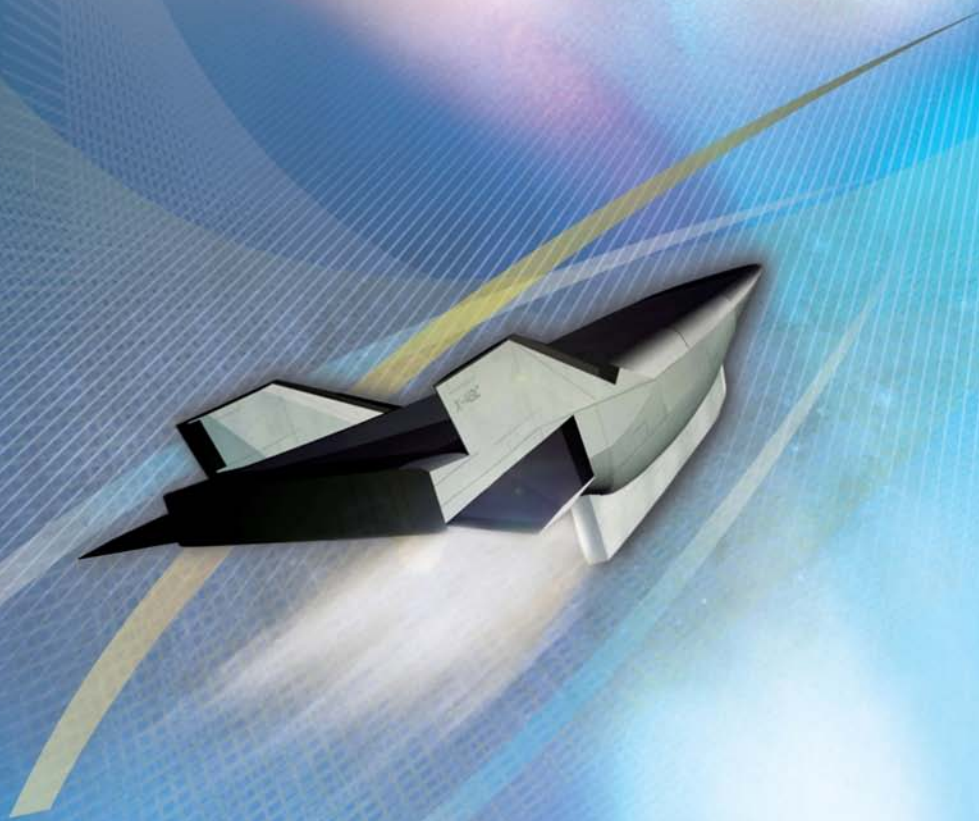


HYPersonic AND HIGH TEMPERATURE GAS DYNAMICS

SECOND EDITION

John D. Anderson Jr.



AMERICAN INSTITUTE OF
AERONAUTICS AND ASTRONAUTICS

AIAA EDUCATION SERIES
JOSEPH A. SCHETZ
EDITOR-IN-CHIEF

Hypersonic and High-Temperature Gas Dynamics

Second Edition

This page intentionally left blank

Hypersonic and High-Temperature Gas Dynamics

Second Edition

John D. Anderson, Jr.

National Air and Space Museum
Smithsonian Institution
Washington, DC
and

Professor Emeritus, Aerospace Engineering
University of Maryland
College Park, Maryland



EDUCATION SERIES

Joseph A. Schetz
Series Editor-in-chief
Virginia Polytechnic Institute and State University
Blacksburg, Virginia

Published by the
American Institute of Aeronautics and Astronautics, Inc.
1801 Alexander Bell Drive, Reston, Virginia 20191-4344

American Institute of Aeronautics and Astronautics, Inc., Reston, Virginia

1 2 3 4 5

Library of Congress Cataloging-in-Publication Data

Anderson, John David.

Hypersonic and high-temperature gas dynamics / John D. Anderson, Jr. -- 2nd ed.

p. cm.

Includes bibliographical references and index.

ISBN-13: 978-1-56347-780-5 (alk. paper)

ISBN-10: 1-56347-780-7 (alk. paper)

1. Aerodynamics, Hypersonic. I. Title

TL571.5.A53 2006

629.132'306--dc22

2006025724

Copyright © 2006 by John D. Anderson, Jr. All rights reserved. Printed in the United States of America. No part of this publication may be reproduced, distributed, or transmitted, in any form or by any means, or stored in a database or retrieval system, without the prior written permission of the publisher.

Data and information appearing in this book are for information purposes only. AIAA is not responsible for any injury or damage resulting from use or reliance, nor does AIAA warrant that use or reliance will be free from privately owned rights.

**To Sarah-Allen, Katherine, and Elizabeth Anderson, for all their
love and understanding**

This page intentionally left blank

AIAA Education Series

Editor-in-Chief

Joseph A. Schetz

Virginia Polytechnic Institute and State University

Editorial Board

Takahira Aoki
University of Tokyo

Rakesh K. Kapania
*Virginia Polytechnic Institute
and State University*

Edward W. Ashford

Brian Landrum
*University of Alabama
Huntsville*

Karen D. Barker
Brahe Corporation

Robert H. Bishop
University of Texas at Austin

Timothy C. Lieuwen
Georgia Institute of Technology

Claudio Bruno
University of Rome

Michael Mohaghegh
The Boeing Company

Aaron R. Byerley
U.S. Air Force Academy

Conrad F. Newberry
Naval Postgraduate School

Richard Colgren
University of Kansas

Mark A. Price
Queen's University Belfast

Kajal K. Gupta
*NASA Dryden Flight Research
Center*

James M. Rankin
Ohio University

Rikard B. Heslehurst
*Australian Defence Force
Academy*

David K. Schmidt
*University of Colorado
Colorado Springs*

David K. Holger
Iowa State University

David M. Van Wie
Johns Hopkins University

This page intentionally left blank

Foreword

It is a great personal pleasure for me to welcome the Second Edition of *Hypersonic and High Temperature Gas Dynamics* by John D. Anderson to the AIAA Education Series. I have known John Anderson for more years than either he or I are comfortable recalling, and I have always found him to be extremely articulate and insightful. The original edition published by McGraw-Hill in 1989 was a very well received, comprehensive, and in-depth treatment of these important topics, and it was reprinted by AIAA in 2000. This new edition has updated the material and expanded the coverage, and we anticipate that it will be equally well received, especially since hypersonics is now enjoying a resurgence of interest. This edition has 18 chapters divided into three main parts and more than 800 pages.

John Anderson is very well-qualified to write this book, first because of his broad and deep expertise in the area. Second, his command of the material is excellent, and he is able to organize and present it in a very clear manner. In addition, John writes in a very readable style, which has made all of his books popular with both students and working professionals. Finally, John Anderson has long played a key role in AIAA publications activities, including books and journal papers, as well as leadership roles, and that makes us particularly pleased to have this book under the AIAA masthead.

The AIAA Education Series aims to cover a very broad range of topics in the general aerospace field, including basic theory, applications and design. A complete list of titles can be found at <http://www.aiaa.org>. The philosophy of the series is to develop textbooks that can be used in a university setting, instructional materials for continuing education and professional development courses, and also books that can serve as the basis for independent study. Suggestions for new topics or authors are always welcome.

Joseph A. Schetz
Editor-in-Chief
AIAA Education Series

This page intentionally left blank

Table of Contents

Preface to the Second Edition xvii

Preface to the First Edition xix

Chapter	1. Some Preliminary Thoughts	1
1.1	Hypersonic Flight—Some Historical Firsts	2
1.2	Hypersonic Flow—Why Is It Important?	5
1.3	Hypersonic Flow—What Is It?	13
1.4	Fundamental Sources of Aerodynamic Force and Aerodynamic Heating	23
1.5	Hypersonic Flight Paths: Velocity-Altitude Map	27
1.6	Summary and Outlook	29
	Problems	31

Part 1. Inviscid Hypersonic Flow

Chapter	2. Hypersonic Shock and Expansion-Wave Relations	35
2.1	Introduction	36
2.2	Basic Hypersonic Shock Relations	36
2.3	Hypersonic Shock Relations in Terms of the Hypersonic Similarity Parameter	42
2.4	Hypersonic Expansion-Wave Relations	44
2.5	Summary and Comments	47
	Problem	49

Chapter	3. Local Surface Inclination Methods	51
3.1	Introduction	52
3.2	Newtonian Flow	54
3.3	Modified Newtonian Law	61
3.4	Centrifugal Force Corrections to Newtonian Theory	63
3.5	Newtonian Theory—What It Really Means	70
3.6	Tangent-Wedge Tangent-Cone Methods	79
3.7	Shock-Expansion Method	83
3.8	Summary and Comments	86

	Design Example 3.1	87
	Problems	100
Chapter	4. Hypersonic Inviscid Flowfields: Approximate Methods	103
4.1	Introduction	104
4.2	Governing Equations	106
4.3	Mach-Number Independence	107
4.4	Hypersonic Small-Disturbance Equations	111
4.5	Hypersonic Similarity.	118
4.6	Hypersonic Small-Disturbance Theory: Some Results	129
4.7	Comment on Hypersonic Small-Disturbance Theory	145
4.8	Hypersonic Equivalence Principle and Blast-Wave Theory.	146
4.9	Thin Shock-Layer Theory	167
4.10	Summary and Comments	173
	Problems	176
Chapter	5. Hypersonic Inviscid Flowfields: Exact Methods	179
5.1	General Thoughts	182
5.2	Method of Characteristics	184
5.3	Time-Marching Finite Difference Method: Application to the Hypersonic Blunt-Body Problem	199
5.4	Correlations for Hypersonic Shock-Wave Shapes	222
5.5	Shock-Shock Interactions.	225
5.6	Space-Marching Finite Difference Method: Additional Solutions of the Euler Equations	231
5.7	Comments on the State of the Art	246
5.8	Summary and Comments	247
	Design Example 5.1	247
	Design Example 5.2: Hypersonic Waveriders—Part 1	250
	Problems	257

Part 2. Viscous Hypersonic Flow

Chapter	6. Viscous Flow: Basic Aspects, Boundary Layer Results, and Aerodynamic Heating	261
6.1	Introduction	262
6.2	Governing Equations for Viscous Flow: Navier–Stokes Equations.	266
6.3	Similarity Parameters and Boundary Conditions	268
6.4	Boundary-Layer Equations for Hypersonic Flow.	272
6.5	Hypersonic Boundary-Layer Theory: Self-Similar Solutions	278
6.6	Nonsimilar Hypersonic Boundary Layers	315
6.7	Hypersonic Transition	327

6.8	Hypersonic Turbulent Boundary Layer	335
6.9	Reference Temperature Method	341
6.10	Hypersonic Aerodynamic Heating: Some Comments and Approximate Results Applied to Hypersonic Vehicles	346
6.11	Entropy-Layer Effects on Aerodynamic Heating	353
6.12	Summary and Comments	355
	Design Example 6.1	358
	Design Example 6.2: Hypersonic Waveriders—Part 2	361
	Problems	374
Chapter	7. Hypersonic Viscous Interactions	375
7.1	Introduction	376
7.2	Strong and Weak Viscous Interactions: Definition and Description	380
7.3	Role of $\bar{\chi}$ in Hypersonic Viscous Interaction	382
7.4	Other Viscous Interaction Results	389
7.5	Hypersonic Shock-Wave/Boundary-Layer Interactions	395
7.6	Summary and Comments	407
	Design Example 7.1: Hypersonic Waveriders—Part 3	409
	Problems	413
Chapter	8. Computational-Fluid-Dynamic Solutions of Hypersonic Viscous Flows	415
8.1	Introduction	416
8.2	Viscous Shock-Layer Technique	418
8.3	Parabolized Navier–Stokes Solutions	424
8.4	Full Navier–Stokes Solutions	434
8.5	Summary and Comments	444
Part 3. High-Temperature Gas Dynamics		
Chapter	9. High-Temperature Gas Dynamics: Some Introductory Considerations	449
9.1	Importance of High-Temperature Flows	450
9.2	Nature of High-Temperature Flows	458
9.3	Chemical Effects in Air: The Velocity-Altitude Map	459
9.4	Summary and Comments	461
Chapter	10. Some Aspects of the Thermodynamics of Chemically Reacting Gases (Classical Physical Chemistry)	463
10.1	Introduction: Definition of Real Gases and Perfect Gases	464
10.2	Various Forms of the Perfect-Gas Equation of State	466
10.3	Various Descriptions of the Composition of a Gas Mixture	472

10.4	Classification of Gases	474
10.5	First Law of Thermodynamics	478
10.6	Second Law of Thermodynamics	481
10.7	Calculation of Entropy	483
10.8	Gibbs Free Energy and the Entropy Produced by Chemical Nonequilibrium	485
10.9	Composition of Equilibrium Chemically Reacting Mixtures: The Equilibrium Constant	488
10.10	Heat of Reaction	495
10.11	Summary and Comments	497
	Problems	499
Chapter 11.	Elements of Statistical Thermodynamics	501
11.1	Introduction	502
11.2	Microscopic Description of Gases	503
11.3	Counting the Number of Microstates for a Given Macrostate	512
11.4	Most Probable Macrostate	514
11.5	Limiting Case: Boltzmann Distribution	516
11.6	Evaluation of Thermodynamic Properties in Terms of the Partition Function	518
11.7	Evaluation of the Partition Function in Terms of T and V	524
11.8	Practical Evaluation of Thermodynamic Properties for a Single Chemical Species	528
11.9	Calculation of the Equilibrium Constant	532
11.10	Chemical Equilibrium—Some Further Comments	537
11.11	Calculation of the Equilibrium Composition for High-Temperature Air	538
11.12	Thermodynamic Properties of an Equilibrium Chemically Reacting Gas	542
11.13	Equilibrium Properties of High-Temperature Air	547
11.14	Summary and Comments	557
	Problems	558
Chapter 12.	Elements of Kinetic Theory	559
12.1	Introduction	560
12.2	Perfect-Gas Equation of State (Revisited)	560
12.3	Collision Frequency and Mean Free Path	564
12.4	Velocity and Speed Distribution Functions: Mean Velocities	567
12.5	Summary and Comments	571
	Problems	573
Chapter 13.	Chemical and Vibrational Nonequilibrium	575
13.1	Introduction	576

13.2	Vibrational Nonequilibrium: The Vibrational Rate Equation	577
13.3	Chemical Nonequilibrium: The Chemical Rate Equation.	584
13.4	Chemical Nonequilibrium in High-Temperature Air.	590
13.5	Chemical Nonequilibrium in H ₂ -Air Mixtures	595
13.6	Summary and Comments	597
Chapter 14. Inviscid High-Temperature Equilibrium Flows		599
14.1	Introduction	600
14.2	Governing Equations for Inviscid High-Temperature Equilibrium Flow	601
14.3	Equilibrium Normal and Oblique Shock-Wave Flows.	604
14.4	Equilibrium Quasi-One-Dimensional Nozzle Flows	617
14.5	Frozen and Equilibrium Flows: The Distinction	623
14.6	Equilibrium and Frozen Specific Heats	626
14.7	Equilibrium Speed of Sound	629
14.8	Equilibrium Conical Flow	633
14.9	Equilibrium Blunt-Body Flows	636
14.10	Summary and Comments	643
	Design Example 14.1: Hypersonic Waveriders—Part 4	644
	Problems	646
Chapter 15. Inviscid High-Temperature Nonequilibrium Flows		647
15.1	Introduction	648
15.2	Governing Equations for Inviscid, Nonequilibrium Flows	649
15.3	Nonequilibrium Normal and Oblique Shock-Wave Flows	655
15.4	Nonequilibrium Quasi-One-Dimensional Nozzle Flows	663
15.5	Nonequilibrium Blunt-Body Flows	671
15.6	Binary Scaling	680
15.7	Nonequilibrium Flow over Other Shapes: Nonequilibrium Method of Characteristics.	683
15.8	Summary and Comments	687
	Problems	690
Chapter 16. Kinetic Theory Revisited: Transport Properties in High-Temperature Gases		691
16.1	Introduction	692
16.2	Definition of Transport Phenomena	692
16.3	Transport Coefficients.	696
16.4	Mechanism of Diffusion	700
16.5	Energy Transport by Thermal Conduction and Diffusion: Total Thermal Conductivity	702
16.6	Transport Properties for High-Temperature Air.	705
16.7	Summary and Comments	709

Chapter 17. Viscous High-Temperature Flows	711
17.1 Introduction	712
17.2 Governing Equations for Chemically Reacting Viscous Flow	712
17.3 Alternate Forms of the Energy Equation	715
17.4 Boundary-Layer Equations for a Chemically Reacting Gas	719
17.5 Boundary Conditions: Catalytic Walls	726
17.6 Boundary-Layer Solutions: Stagnation-Point Heat Transfer for a Dissociating Gas	729
17.7 Boundary-Layer Solutions: Nonsimilar Flows	739
17.8 Viscous-Shock-Layer Solutions to Chemically Reacting Flow	741
17.9 Parabolized Navier–Stokes Solutions to Chemically Reacting Flows	749
17.10 Full Navier–Stokes Solutions to Chemically Reacting Flows	751
17.11 Summary and Comments	756
Problems	756
Chapter 18. Introduction to Radiative Gas Dynamics	759
18.1 Introduction	760
18.2 Definitions of Radiative Transfer in Gases	760
18.3 Radiative-Transfer Equation	763
18.4 Solutions of the Radiative-Transfer Equation: Transparent Gas	765
18.5 Solutions of the Radiative-Transfer Equation: Absorbing Gas	768
18.6 Solutions of the Radiative-Transfer Equation: Emitting and Absorbing Gas	769
18.7 Radiating Flowfields: Sample Results	773
18.8 Surface Radiative Cooling	780
18.9 Summary and Comments	781
Design Example 18.1	782
Problems	785
Postface	787
References	789
Index	805
Supporting Materials	813

Preface to the Second Edition

Almost 20 years have passed since the publication of the first edition of this book. During those 20 years, much progress has been made in hypersonic and high-temperature gas dynamics, principally in the extensive use of sophisticated modern computational fluid dynamics and in the design of serious flight hardware. The physical and mathematical fundamentals of hypersonic and high-temperature gas dynamics, however, have by their very nature remained the same.

This book is about the *fundamentals*, which have not changed. Therefore, almost all of the content of the first edition has been carried over the present edition. Indeed, now is a good moment to pause and read the preface of the first edition. Everything said there is appropriate to the second edition. For example, the book remains a self-contained teaching instrument for those students and readers interested in learning hypersonic and high-temperature gas dynamics starting with the basics. This book assumes no prior familiarity with either subject on the part of the reader. If you have never studied hypersonic and/or high-temperature gas dynamics and if you have never worked in the area, *then this book is for you*. On the other hand, if you have worked and/or are working in these areas and you want a cohesive presentation of the fundamentals, a development of important theory and techniques, a discussion of salient results with emphasis on the physical aspects, and a presentation of modern thinking in these areas, *then this book is also for you*.

As with the first edition, this second edition is written in an informal, conversational style. This book *talks to you*, just as if you and I were sitting down together at a table discussing the subject matter. I want you to have fun learning these topics. This is not difficult because the areas of hypersonic and high-temperature gas dynamics are full of interesting and exciting phenomena and applications.

What is new and different about the second edition? A lot! Much new material has been added to accomplish two purposes, namely, to bring the book up to date and to enhance even further the pedagogical goal of helping the reader to learn. For example:

1) A lot of new literature has been published in the discipline over the past 20 years. This new edition draws from the modern literature in order to update the presentations. This is not a book about the state of the art—it is about fundamentals. But the state of the art is used to reinforce the fundamentals.

2) The topic of shock-shock interactions, particularly the important type-IV interaction, has been added as a new extensive section in Chapter 5.

3) Although this book emphasizes the fundamentals, modern hypersonic and high-temperature gas dynamics is moving more and more toward design of viable systems. Therefore, this edition has a design flavor not present in the first edition. At the back of a number of chapters, design examples that illustrate the application of the fundamentals to methods of design are added. A number of these design examples focus on different aspect of hypersonic waverider design. Waveriders were not treated in the first edition. Because they are an interesting configuration for possible future hypersonic vehicles they are extensively treated here.

4) Chapter previews have been added at the beginning of most of the chapters. These are pedagogical tools to provide the reader with insight about what each chapter is about and why the material is so important. They are written in a particularly informal manner—plain speaking—to help turn the reader on to the content. In these previews I am unabashedly admitting to providing some fun for the readers.

5) Road maps have been placed at the beginning of almost every chapter to help guide the reader through the logical flow of the material—another pedagogical tool to enhance the *self-learning nature* of this book.

Special thanks go to Rodger Williams of the AIAA for suggesting, encouraging, and essentially commissioning this second edition, and with whom it is always a pleasure to work, and to the entire AIAA publications team who have always made me feel like one of them. Thanks also to Susan Cunningham who typed the original manuscript of the first edition 20 years ago and who received the call again for the added material for the second edition.

Finally, I want to acknowledge in a very special way the late Rudolph Edse, my mentor and advisor at The Ohio State University, who gave me the true appreciation for the fundamentals, and Dr. John D. Lee and the rest of the faculty of the Department of Aeronautical and Astronautical Engineering at Ohio State during the 1960s who taught me all there was to know about hypersonic flow.

John D. Anderson, Jr.

July 2006

Preface to the First Edition

This book is designed to be a self-contained *teaching instrument* for those students and readers interested in learning hypersonic flow and high-temperature gas dynamics. It assumes no prior familiarity with either subject on the part of the reader. If you have never studied hypersonic and/or high-temperature gas dynamics before, and if you have never worked extensively in the area, *then this book is for you*. On the other hand, if you have worked and/or are working in these areas, and you want a cohesive presentation of the fundamentals, a development of important theory and techniques, a discussion of the salient results with emphasis on the physical aspects, and a presentation of modern thinking in these areas, *then this book is also for you*. In other words, this book is aimed for two roles: 1) as an effective classroom text, which can be used with ease by the instructor and which can be understood with ease by the student; and 2) as a viable, professional working tool on the desk of all engineers, scientists, and managers who have any contact in their jobs with hypersonic and/or high-temperature flow.

The only background assumed on the part of the reader is a basic knowledge of undergraduate fluid dynamics, including a basic introductory course on compressible flow; that is, the reader is assumed to be familiar with material exemplified by two of the author's previous books, namely, *Fundamentals of Aerodynamics* (McGraw-Hill, 1984), and the first half of *Modern Compressible Flow: with Historical Perspective* (McGraw-Hill, 1982). Indeed, throughout the present book, frequent reference is made to basic material presented in these two books. Finally, the present book is pitched at the advanced senior and first-year graduate levels and is designed to be used in the classroom as the main text for courses at these levels in hypersonic flow and high-temperature gas dynamics. Homework problems are given at the ends of most chapters in order to enhance its use as a teaching instrument.

Hypersonic aerodynamics is an important part of the entire flight spectrum, representing the segment at the extreme high velocity of this spectrum. Interest in hypersonic aerodynamics grew in the 1950s and 1960s with the advent of hypersonic atmospheric entry vehicles, especially the manned space program as represented by Mercury, Gemini, and Apollo. Today, many new, exciting vehicle concepts involving hypersonic flight are driving renewed and, in some cases, frenzied interest in hypersonics. Such new concepts are described in Chapter 1. This book is a response to the need to provide a basic education in hypersonic and high-temperature gas dynamics for a new generation of engineers

and scientists, as well as to provide a basic discussion of these areas from a modern perspective. Six texts in hypersonic flow were published before 1966; the present book is the first basic classroom text to become available since then. Therefore, the present book is intended to make up for this 20-year hiatus and to provide a *modern* education in hypersonic and high-temperature gas dynamics, while discussing at length the basic fundamentals.

To enhance the reader's understanding and to peak his or her interest, the present book is written in the style of the author's previous ones, namely, it is intentionally written in an informal, conversational style. The author wants the reader to *have fun* while learning these topics. This is not difficult because the areas of hypersonic and high-temperature gas dynamics are full of interesting and exciting phenomena and applications.

The present book is divided into three parts. Part 1 deals with inviscid hypersonic flow, emphasizing purely the fluid-dynamic effects of the Mach number becoming large. High-temperature effects are not included. Part 2 deals with viscous hypersonic flow, emphasizing the purely fluid-dynamic effects of including the transport phenomena of viscosity and thermal conduction at the same time that the Mach number becomes large. High-temperature effects are not included. Finally, Part 3 deals with the influence of high temperatures on both inviscid and viscous flows. In this fashion, the reader is led in an organized fashion through the various physical phenomena that dominate high-speed aerodynamics. To further enhance the organization of the material, the reader is given a "road map" in Fig. 1.24 to help guide his or her thoughts as we progress through our discussions.

When this book was first started, the author's intent was to have a Part 4, which would cover the miscellaneous but important topics of low-density flows, experimental hypersonics, and applied aerodynamics associated with hypersonic vehicle design. During the course of writing this book, it quickly became apparent that including Part 4 would vastly exceed the length constraints allotted to this book. Therefore, the preceding matters are not considered in any detail here. This is not because of a lack of importance of such material, but rather because of an effort to emphasize the basic fundamentals in the present book. Therefore, Parts 1, 2, and 3 are sufficient; they constitute the essence of a necessary fundamental background in hypersonic and high-temperature gas dynamics. The material of the missing Part 4 will have to wait for another time.

The content of this book is influenced in part by the author's experience in teaching such material in courses at the University of Maryland. It is also influenced by the author's three-day short course on the introduction to hypersonic aerodynamics, which he has had the privilege to give at 10 different laboratories, companies, and universities over the past year. These experiences have fine tuned the present material in favor of what the reader wants to know and what he or she is thinking.

Several organizations and people are owed the sincere thanks of the author in aiding the preparation of this book. First, the author is grateful to the National Air and Space Museum of the Smithsonian Institution where he spent an enlightening sabbatical year during 1986–1987 as the Charles Lindbergh Professor in the Aeronautics Department. A substantial portion of this book was written during that sabbatical year at the museum. Secondly, the author is grateful to

PREFACE TO THE FIRST EDITION

xxi

the University of Maryland for providing the intellectual atmosphere conducive to scholarly projects. Also, many thanks go to the author's graduate students in the hypersonic aerodynamics program at Maryland—thanks for the many enlightening discussions on the nature of hypersonic and high-temperature flows. For the mechanical preparation of this manuscript, the author has used his own word processor named Susan O. Cunningham—a truly "human" human being who has typed the manuscript with the highest professional standards. Finally, once again the author is grateful for the support at home provided by the Anderson family, who allowed him to undertake this project in the first place, and for joining him in the collective sigh of relief upon its completion.

I would like to express my thanks for the many useful comments and suggestions provided by colleagues who reviewed this text during the course of its development, especially to Judson R. Baron, Massachusetts Institute of Technology; Daniel Bershadter, Stanford University; John D. Lee, Ohio State University; and Maurice L. Rasmussen, University of Oklahoma.

John D. Anderson, Jr.

October 1987

This page intentionally left blank

3**Local Surface Inclination Methods**

Newton's ideas are as old as reason and as new as research.

*J. C. Hunsaker, comments to the Royal Society,
Cambridge, England, at the occasion of
the Newton Tercentenary Celebration, July 1946*

A striking difference between linear and nonlinear waves concerns the phenomenon of interaction: the principle of superposition holds for linear waves but not for nonlinear waves. As a consequence, for example, excess pressures of interfering sound waves are merely additive: in contrast to this fact, interaction and reflection of nonlinear waves may lead to enormous increases in pressure.

Richard Courant and K. O. Fredericks, 1948

Chapter Preview

The calculation of surface-pressure distributions over hypersonic bodies—that is the exclusive name of the game for this chapter. The resulting aerodynamic lift and wave drag are also treated here. This is our first opportunity in this book to calculate such pressure distribution and aerodynamic forces. And we do it in the quickest and easiest way possible by cutting directly to the body surface, calculating the pressure there, but nowhere else in the flowfield. All we need to know to calculate the pressure at a point on the surface of a body in a given hypersonic freestream is the local inclination angle the surface makes at that point with the freestream direction. Sounds very straightforward, does it not? But there is no free lunch here. We pay for this simplicity by sacrificing accuracy. How much? We will see. We will also see that the several methods discussed here are incredibly simple and straightforward.

52 HYPersonic AND HIGH-TEMPERATURE GAS DYNAMICS

These simple methods are grouped under the heading of “local surface inclination methods,” for obvious reasons. In the early days of hypersonic aerodynamics—in the 1950s—these methods were about the only thing going. This is how aeronautical engineers in those days made estimates of surface pressures for the design of hypersonic vehicles. Today, in the world of modern computational fluid dynamics and very sophisticated calculations of complete flowfields around hypersonic bodies, the material in this chapter takes on the role of “back-of-the-envelope” calculations. This is the modern value of the methods discussed here—for you to carry them around in the pocket of your mind so that you can whip them out at any time to make a quick estimate of hypersonic pressure distributions, lift, and wave drag. These methods can be used as reality checks in the world of hypersonic vehicle design and performance.

This chapter is a great way to get off the ground in learning hypersonic aerodynamics. It is straightforward and to the point. It gives you some immediate tools to work with and allows you to make some fun calculations. So read on and have fun.

3.1 Introduction

Hypersonic flow is inherently *nonlinear*. This is intuitively obvious when we think of the important physical aspects of hypersonics discussed in Chapter 1—aspects such as high-temperature chemically reacting flows, viscous interaction, entropy layers, etc. It is hard to imagine that such complex phenomena could be described by simple linear relationships. Even without these considerations, the basic theory of inviscid compressible flow, when the Mach number becomes large, does not yield aerodynamic theories that are mathematically linear. This is in stark contrast to supersonic flow, which, for thin bodies at small angles of attack, can be described by a linear partial differential equation, leading to the familiar supersonic expression for pressure coefficient on a surface (or stream-line) with local deflection angle θ :

$$C_p = \frac{2\theta}{\sqrt{M_\infty^2 - 1}} \quad (3.1)$$

In Eq. (3.1), M_∞ is the freestream Mach number. Equation (3.1) is a classic result from inviscid, linearized, two-dimensional, supersonic flow theory (for example, see [4] and [5]). It is simple and easy to apply. Unfortunately, it is **not valid at hypersonic speeds**, for reasons to be discussed in Chapter 4.

A virtue of Eq. (3.1) is that for a specified freestream Mach number it gives the pressure coefficient on the surface of a body strictly in terms of the *local deflection angle of the surface* θ . That is, within the framework of supersonic linearized theory, C_p at any point on a body does *not* depend on the details of the flowfield away from that point; thus, it does *not* require a detailed solution

LOCAL SURFACE INCLINATION METHODS

53

of the complete flowfield. In essence, Eq. (3.1) provides a *local surface inclination method* for the prediction of pressure distributions over two-dimensional supersonic bodies (restricted to thin bodies at small angles of attack). Such simplicity is always welcomed by practicing aerodynamicists who have to design flight vehicles. This leads to the question: although hypersonic aerodynamics is nonlinear, and hence Eq. (3.1) does not hold, are there other methods, albeit approximate, that allow the rapid estimate of pressure distributions over hypersonic bodies just in terms of the local surface inclination angle? In other words, is there a viable *local surface inclination method for hypersonic applications*? The answer is *yes*; indeed, there are several such methods that apply to hypersonic bodies. The purpose of this chapter is to present these methods.

Finally, examine the road map given in Fig. 1.24. Note that the material discussed in Chapter 2, as well as the present chapter, is itemized on the far left side of the road map. Keep in mind that we are still discussing inviscid hypersonic flow, where essentially we are examining the purely fluid-dynamic effect of large Mach numbers.

Also, a more detailed road map for the present chapter is given in Fig. 3.1. We begin with Newtonian flow, a classic fluid-dynamic theory postulated by Isaac Newton in 1687, which resulted in very poor accuracy for low-speed fluid-dynamic applications over the subsequent centuries. Only with the advent of modern hypersonic aerodynamic applications has Newtonian theory really come into its own. Newtonian theory provides the most straightforward and simplest prediction of surface pressure on a hypersonic body. That is why we start with it here. Moreover, we will explore several aspects of Newtonian flow as itemized in the subheadings in Fig. 3.1. Two other primary methods for the

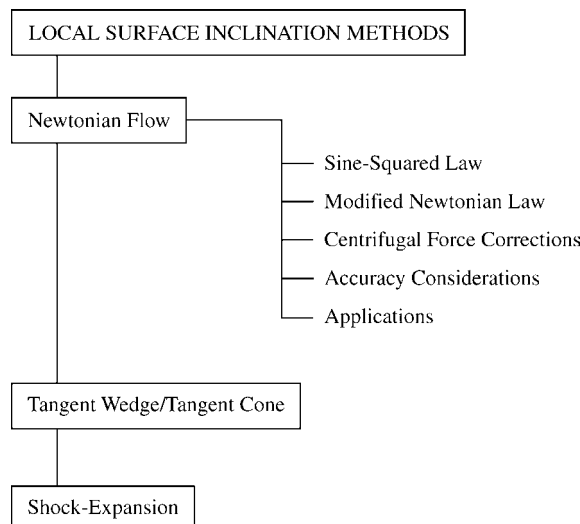


Fig. 3.1 Road map for Chapter 3.

54 HYPersonic AND HIGH-TEMPERATURE GAS DYNAMICS

direct calculation of surface pressure on a hypersonic body are also listed in Fig. 3.1, namely, the tangent-wedge/tangent-cone and the shock-expansion methods. These methods are slightly more elaborate than Newtonian, but provide inherently better accuracy. The road map for this chapter, Fig. 3.1, is relatively short and straightforward, but it is worthwhile to keep it in mind as you progress through the chapter.

3.2 Newtonian Flow

Three centuries ago, Isaac Newton established a fluid-dynamic theory that later was used to derive a “law” for the force on an inclined plane in a moving fluid. This law indicated that the force varies as the square of the sine of the deflection angle—the famous Newtonian sine-squared law. Experimental investigations carried out by d'Alembert more than a half-century later indicated that Newton's sine-squared law was not very accurate, and, indeed, the preponderance of fluid-dynamic experience up to the present day confirms this finding. The exception to this is the modern world of hypersonic aerodynamics. Ironically, Newtonian theory, developed 300 years ago for the application to low-speed fluid dynamics, has direct application to the prediction of pressure distributions on hypersonic bodies. What is the application and why? The answers are the subject of this section.

In propositions 34 and 35 of his *Principia*, first published in 1687, Newton modeled a fluid flow as a stream of particles in rectilinear motion, much like a stream of pellets from a shotgun blast, which, when striking a surface, would lose all of their momentum normal to the surface but would move tangentially to the surface without loss of tangential momentum. This picture is illustrated in Fig. 3.2, which shows a stream with velocity V_∞ impacting on a surface of area A inclined at the angle θ to the freestream. From this figure, we see that

$$(\text{Change in normal velocity}) = V_\infty \sin \theta$$

$$\{\text{Mass flux incident on a surface area } A\} = \rho_\infty V_\infty A \sin \theta$$

{Time rate of change of

$$\begin{aligned} \{\text{momentum of this mass flux}\} &= (\rho_\infty V_\infty A \sin \theta)(V_\infty \sin \theta) \\ &= \rho_\infty V_\infty^2 A \sin^2 \theta \end{aligned}$$

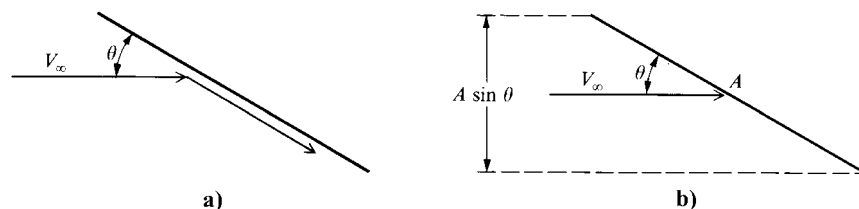


Fig. 3.2 Schematic for Newtonian impact theory.

LOCAL SURFACE INCLINATION METHODS

55

From Newton's second law, the time rate of change of momentum is equal to the force F exerted on the surface

$$F = \rho_\infty V_\infty^2 A \sin^2 \theta$$

or

$$\frac{F}{A} = \rho_\infty V_\infty^2 \sin^2 \theta \quad (3.2)$$

The force F in Eq. (3.2) requires some interpretation. Newton assumed the stream of particles to be rectilinear, that is, he assumed that the individual particles do not interact with each other, and have no random motion. Because of this lack of random motion, F in Eq. (3.2) is a force associated only with the directed linear motion of the particles. On the other hand, modern science recognizes that the static pressure of a gas or liquid is a result of the purely random motion of the particles—motion not included in Newtonian theory. Hence, in Eq. (3.2), F/A , which has the dimensions of pressure, must be interpreted as the pressure *difference* above the freestream static pressure, namely,

$$\frac{F}{A} = p - p_\infty$$

where p is the surface pressure and p_∞ is the freestream static pressure. Hence, from Eq. (3.2)

$$p - p_\infty = \rho_\infty V_\infty^2 \sin^2 \theta$$

or

$$\frac{p - p_\infty}{\frac{1}{2} \rho_\infty V_\infty^2} = 2 \sin^2 \theta$$

or

$C_p = 2 \sin^2 \theta$

(3.3)

Equation (3.3) is the famous Newtonian sine-squared law for pressure coefficient.

What does the Newtonian pressure coefficient have to do with hypersonic flow? To answer this question, recall Fig. 1.13, which illustrated the shock wave and thin shock layer on a 15-deg wedge at Mach 36. An elaboration of this picture is given in Fig. 3.3, which shows the streamline pattern for the same Mach 36 flow over the same wedge. Here, upstream of the shock wave, we see straight, parallel streamlines in the horizontal freestream direction; downstream of the shock wave, the streamlines are also straight but parallel to the wedge surface inclined at a 15-deg angle. Now imagine that you examine

56 HYPERSONIC AND HIGH-TEMPERATURE GAS DYNAMICS

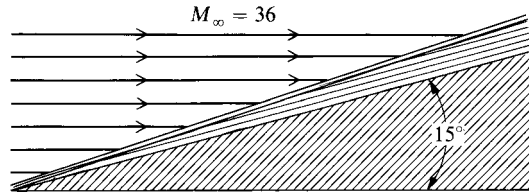


Fig. 3.3 Streamlines in the thin hypersonic shock layer.

Fig. 3.3 from a distance, say, from across the room. Because the shock wave lies so close to the surface at hypersonic speeds, Fig. 3.3 “looks” as if the incoming flow is directly impinging on the wedge surface and then is running parallel to the surface downstream—*precisely the picture Newton drew in 1687*. Therefore, the geometric picture of hypersonic flowfields has some characteristics that closely approximate Newtonian flow; Newton’s model had to wait for more than two-and-a-half centuries before it came into own. By this reasoning, Eq. (3.3) should approximate the surface-pressure coefficient in hypersonic flow. Indeed, it has been used extensively for this purpose since the early 1950s.

In applying Eq. (3.3) to hypersonic bodies, θ is taken as the local deflection angle, that is, the angle between the tangent to the surface and the freestream. Clearly, Newtonian theory is a local surface inclination method, where C_p depends only on the local surface deflection angle; it does not depend on any aspect of the surrounding flowfield. To be specific, consider Fig. 3.4a, which shows an arbitrarily shaped two-dimensional body. Assume that we wish to estimate the pressure at point P on the body surface. Draw a line tangent to the body at point P ; the angle between this line and the freestream is denoted by θ . Hence, from Newtonian theory the value of C_p at this point is given by $C_p = 2 \sin^2 \theta$. Now consider a three-dimensional body such as sketched in Fig. 3.4b. We

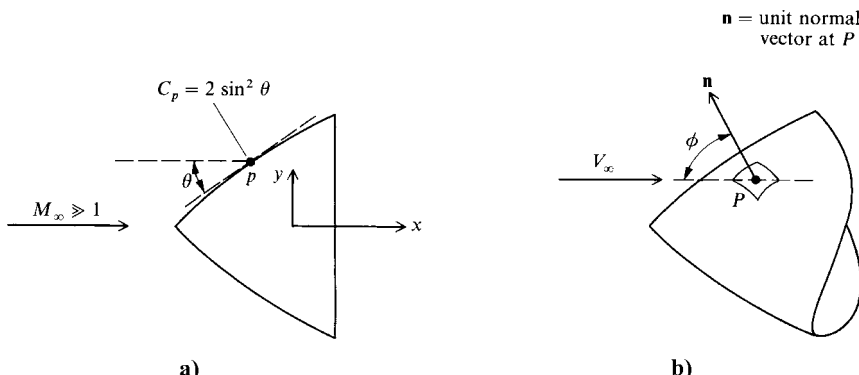


Fig. 3.4 Geometry for Newtonian applications in a) two-dimensional flow and b) three-dimensional flow.

LOCAL SURFACE INCLINATION METHODS

57

wish to estimate the pressure at an arbitrary point P on this body. Draw a unit normal vector \mathbf{n} to the surface at point P . Consider the freestream velocity as a vector \mathbf{V}_∞ . Then, by definition of the vector dot product, and using a trigonometric identity, we obtain

$$\mathbf{V}_\infty \cdot \mathbf{n} = |\mathbf{V}_\infty| \cos \phi = |\mathbf{V}_\infty| \sin\left(\frac{\pi}{2} - \phi\right) \quad (3.4)$$

where ϕ is the angle between \mathbf{n} and \mathbf{V}_∞ . The vectors \mathbf{n} and \mathbf{V}_∞ define a plane, and in that plane the angle $\theta = \pi/2 - \phi$ is the angle between a tangent to the surface and the freestream direction. Thus, from Eq. (3.4)

$$\mathbf{V}_\infty \cdot \mathbf{n} = |\mathbf{V}_\infty| \sin \theta$$

or

$$\sin \theta = \frac{\mathbf{V}_\infty}{|\mathbf{V}_\infty|} \cdot \mathbf{n} \quad (3.5)$$

The Newtonian pressure coefficient at point P on the three-dimensional body is then $C_p = 2 \sin^2 \theta$, where θ is given by Eq. (3.5).

In the Newtonian model of fluid flow, the particles in the freestream impact only on the frontal area of the body; they cannot curl around the body and impact on the backsurface. Hence, for that portion of a body that is in the “shadow” of the incident flow, such as the shaded region sketched in Fig. 3.5, no impact pressure is felt. Hence, over this shadow region it is consistent to assume that $p = p_\infty$, and therefore $C_p = 0$, as indicated in Fig. 3.5.

It is instructive to examine Newtonian theory applied to a flat plate, as sketched in Fig. 3.6. Here, a two-dimensional flat plate with chord length c is at

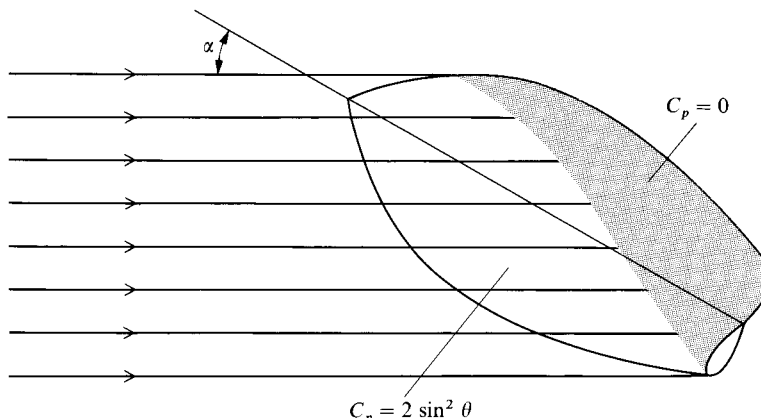


Fig. 3.5 Shadow region on the leeward side of a body, from Newtonian theory.

58 HYPersonic AND HIGH-TEMPERATURE GAS DYNAMICS

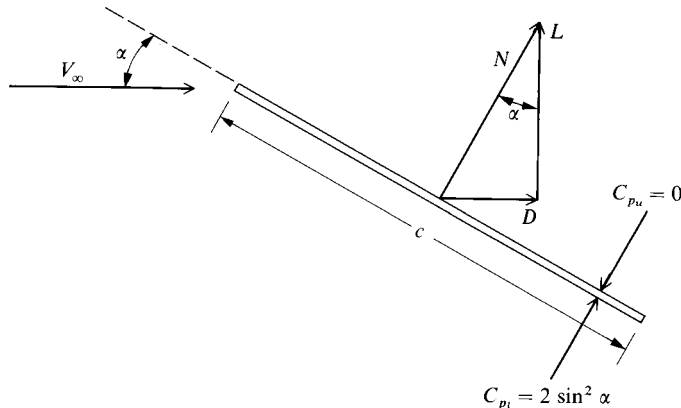


Fig. 3.6 Flat plate at angle of attack. Illustration of aerodynamic forces.

an angle of attack α to the freestream. Because we are not including friction and because surface pressure always acts normal to the surface, the resultant aerodynamic force is perpendicular to the plate, that is, in this case the normal force N is the resultant aerodynamic force. (For an infinitely thin flat plate, this is a general result that is not limited to Newtonian theory or even to hypersonic flow). In turn, N is resolved into lift and drag, denoted by L and D respectively, as shown in Fig. 3.6. According to Newtonian theory, the pressure coefficient on the lower surface is

$$C_{p_l} = 2 \sin^2 \alpha \quad (3.6)$$

and that on the upper surface, which is in the shadow region, is

$$C_{p_u} = 0 \quad (3.7)$$

Defining the normal-force coefficient as $c_n = N/q_\infty S$, where $S = (c)(1)$, we can readily calculate c_n by integrating the pressure coefficients over the lower and upper surfaces (for example, see the derivation given in [5]).

$$c_n = \frac{1}{c} \int_0^c (C_{p_l} - C_{p_u}) dx \quad (3.8)$$

where x is the distance along the chord from the leading edge. Substituting Eqs. (3.6) and (3.7) into (3.8), we obtain

$$c_n = \frac{1}{c} (2 \sin^2 \alpha) c$$

LOCAL SURFACE INCLINATION METHODS

59

or

$$c_n = 2 \sin^2 \alpha \quad (3.9)$$

From the geometry of Fig. 3.6, we see that the lift and drag coefficients, defined as $c_l = L/q_\infty S$ and $c_d = D/q_\infty S$, respectively, where $S = (c)(1)$, are given by

$$c_l = c_n \cos \alpha \quad (3.10)$$

and

$$c_d = c_n \sin \alpha \quad (3.11)$$

Substituting Eq. (3.9) into Eqs. (3.10) and (3.11), we obtain

$$c_l = 2 \sin^2 \alpha \cos \alpha \quad (3.12)$$

and

$$c_d = 2 \sin^3 \alpha \quad (3.13)$$

Finally, from the geometry of Fig. 3.6, the lift-to-drag ratio is given by

$$\frac{L}{D} = \cot \alpha \quad (3.14)$$

[Note that Eq. (3.14) is a general result for inviscid flow over a flat plate. For such flows, the resultant aerodynamic force is the normal force N . From the geometry shown in Fig. 3.6, the resultant aerodynamic force makes the angle α with respect to lift, and clearly, from the right triangle between L , D , and N , we have $L/D = \cot \alpha$. Hence, Eq. (3.14) is not limited to just Newtonian theory.]

The results just obtained above for the application of Newtonian theory to an infinitely thin flat plate are plotted in Fig. 3.7. Here L/D , c_l , and c_d are plotted vs angle of attack α . From this figure, note the following aspects:

1) The value of L/D increases monotonically as α is decreased. Indeed, $L/D \rightarrow \infty$ as $\alpha \rightarrow 0$. However, this is misleading; when skin friction is added to this picture, D becomes finite at $\alpha = 0$, and then $L/D \rightarrow 0$ as $\alpha \rightarrow 0$.

2) The lift curve peaks at about $\alpha \approx 55$ deg. (To be exact it can be shown from Newtonian theory that maximum c_l occurs at $\alpha = 54.7$ deg; the proof of this is left as a homework problem.) It is interesting to note that $\alpha \approx 55$ deg for maximum lift is fairly realistic; the maximum lift coefficient for many practical hypersonic vehicles occurs at angles of attack in this neighborhood.

60 HYPersonic AND HIGH-TEMPERATURE GAS DYNAMICS

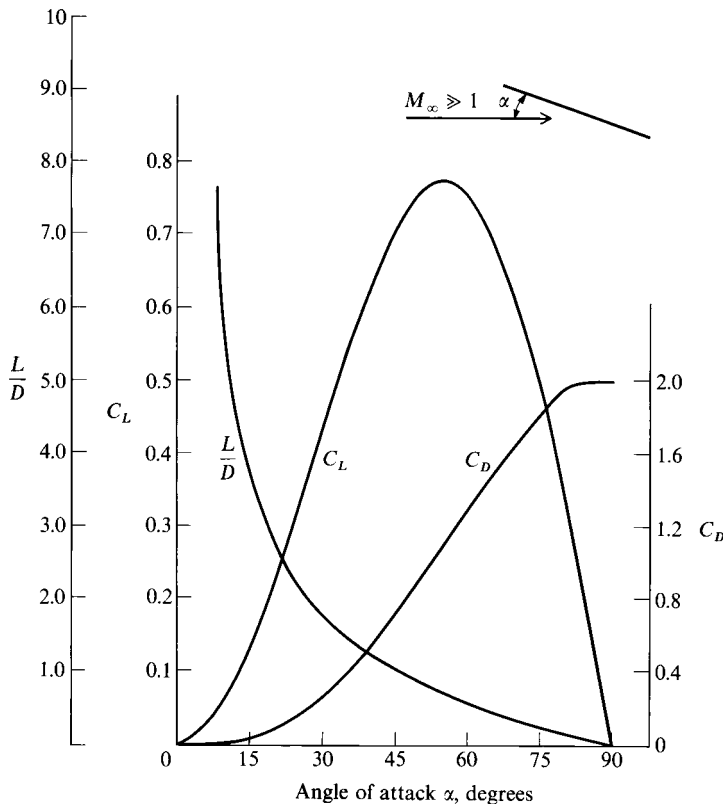


Fig. 3.7 Newtonian results for a flat plate.

3) Examine the lift curve at low angle of attack, say, in the range of α from 0 to 15 deg. Note that the variation of c_l with α is very *nonlinear*. This is in direct contrast to the familiar result for subsonic and supersonic flow, where for thin bodies at small α the lift curve is a linear function of α . (Recall, for example, that the theoretical lift slope from incompressible thin airfoil theory is 2π per radian). Hence, the nonlinear lift curve shown in Fig. 3.7 is a graphic demonstration of the nonlinear nature of hypersonic flow.

Consider two other basic aerodynamic bodies: the circular cylinder of infinite span and the sphere. Newtonian theory can be applied to estimate the hypersonic drag coefficients for these shapes; the results are as follows.

1) Circular cylinder of infinite span:

$$c_d = \frac{D}{q_\infty S}$$

$$S = 2R$$

where R = radius of cylinder,

$$c_d = \frac{4}{3} \quad (\text{from Newtonian theory})$$

2) Sphere:

$$C_D = \frac{D}{q_\infty S}$$

$$S = \pi R^2$$

where R = radius of sphere,

$$C_D = 1 \quad (\text{from Newtonian theory})$$

The derivations of these drag-coefficient values are left for homework problems.

The preceding results from Newtonian theory do not explicitly depend on Mach number. Of course, they implicitly assume that M_∞ is high enough for hypersonic flow to prevail; outside of that, the precise value of M_∞ does not enter the calculations. This is compatible with the *Mach-number independence principle*, to be discussed in Chapter 4. In short, this principle states that certain aerodynamic quantities become relatively independent of Mach number if M_∞ is made sufficiently large. Newtonian results are the epitome of this principle.

3.3 Modified Newtonian Law

Lester Lees [8] proposed a modification to Newtonian theory, writing Eq. (3.3) as

$$C_p = C_{p_{\max}} \sin^2 \theta \quad (3.15)$$

where $C_{p_{\max}}$ is the maximum value of the pressure coefficient, evaluated at a stagnation point behind a normal shock wave, that is,

$$C_{p_{\max}} = \frac{p_{O_2} - p_\infty}{\frac{1}{2} \rho_\infty V_\infty^2} \quad (3.16)$$

where p_{O_2} is the total pressure behind a normal shock wave at the freestream Mach number. From exact normal shock-wave theory, the Rayleigh pitot tube formula gives (see [5])

$$\frac{p_{O_2}}{p_\infty} = \left[\frac{(\gamma + 1)^2 M_\infty^2}{4\gamma M_\infty^2 - 2(\gamma - 1)} \right]^{\gamma/(\gamma-1)} \left[\frac{1 - \gamma + 2\gamma M_\infty^2}{\gamma + 1} \right] \quad (3.17)$$

Noting that $\frac{1}{2} \rho_\infty V_\infty^2 = (\gamma/2) p_\infty M_\infty^2$, Eq. (3.16) becomes

$$C_{p_{\max}} = \frac{2}{\gamma M_\infty^2} \left[\frac{p_{O_2}}{p_\infty} - 1 \right] \quad (3.18)$$

62 HYPersonic AND HIGH-TEMPERATURE GAS DYNAMICS

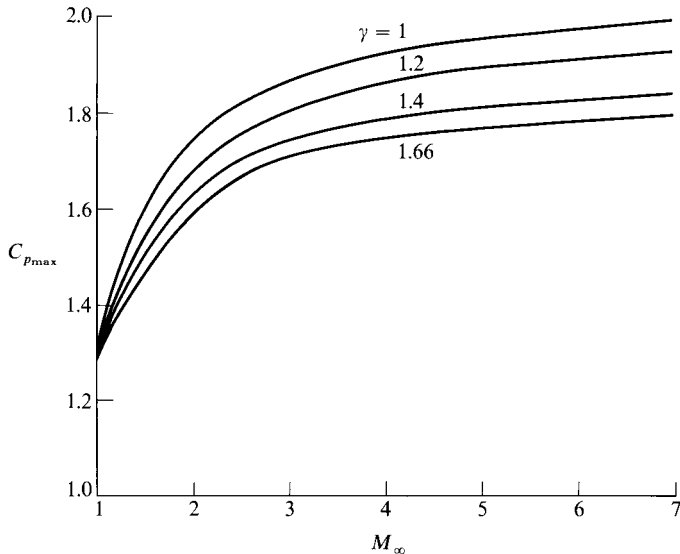


Fig. 3.8 Variation of stagnation-pressure coefficient with M_{∞} and γ .

Combining Eqs. (3.17) and (3.18), we obtain

$$C_{p_{\max}} = \frac{2}{\gamma M_{\infty}^2} \left\{ \left[\frac{(\gamma + 1)^2 M_{\infty}^2}{4\gamma M_{\infty}^2 - 2(\gamma - 1)} \right]^{\gamma/(\gamma-1)} \left[\frac{1 - \gamma + 2\gamma M_{\infty}^2}{\gamma + 1} \right] - 1 \right\} \quad (3.19)$$

This relation is plotted in Fig. 3.8. Note that, in the limit as $M \rightarrow \infty$, we have

$$\begin{aligned} C_{p_{\max}} &\rightarrow \left[\frac{(\gamma + 1)^2}{4\gamma} \right]^{\gamma/(\gamma-1)} \left[\frac{4}{\gamma + 1} \right] \\ &\rightarrow 1.839 \quad \text{for } \gamma = 1.4 \\ &\rightarrow 2.0 \quad \text{for } \gamma = 1 \end{aligned}$$

Equation (3.15), with $C_{p_{\max}}$ given by Eq. (3.19), is called the *modified Newtonian law*. Note the following:

- 1) The modified Newtonian law is no longer Mach-number independent. The effect of a finite Mach number enters through Eq. (3.19).
- 2) As both $M_{\infty} \rightarrow \infty$ and $\gamma \rightarrow 1$, Eqs. (3.15) and (3.19) yield $C_p = 2 \sin^2 \theta$. That is, the straight Newtonian law is recovered in the limit as $M_{\infty} \rightarrow \infty$ and $\gamma \rightarrow 1$.

For the prediction of pressure distributions over blunt-nosed bodies, modified Newtonian, Eq. (3.15), is considerably more accurate than the straight Newtonian, Eq. (3.3). This is illustrated in Fig. 3.9, which shows the pressure distribution over a paraboloid at Mach 8. The solid line is an exact finite-difference

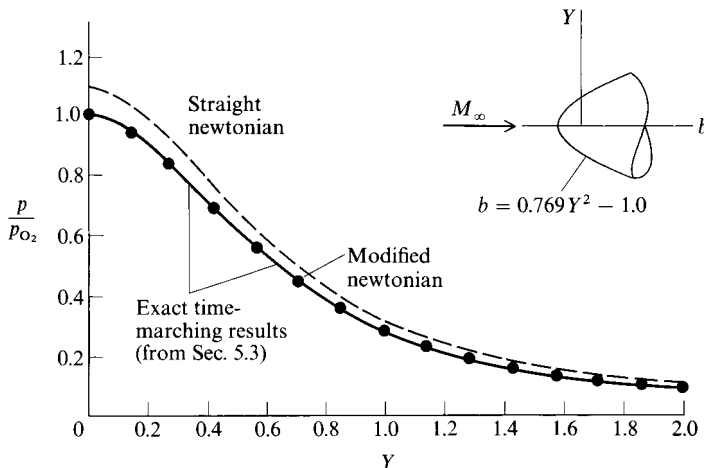


Fig. 3.9 Surface-pressure distribution over a paraboloid at $M_\infty = 8.0$; p_{O_2} is the total pressure behind a normal shock wave at $M_\infty = 8.0$.

solution of the blunt-body flowfield (to be discussed in Chapter 5); the solid symbols are the modified Newtonian results from Eqs. (3.15) and (3.19). Note the excellent agreement, particularly over the forward portion of the nose. The dashed line is the straight Newtonian result from Eq. (3.3); it lies 9% above the exact result. The inspiration for Lester Lee's modification to Newtonian theory appears obvious when examining Fig. 3.9. Clearly, from the proper physics of the flow, the pressure at the stagnation point on the body is equal to the stagnation pressure behind a normal shock wave, that is, the p_{O_2} given by Eq. (3.17); this yields the exact pressure coefficient at the stagnation point, given by Eq. (3.19). Therefore, it is rational to simply replace the coefficient 2 in Eq. (3.3) with the value $C_{p_{\max}}$, as shown in Eq. (3.15). This forces Newtonian theory to be exact at the stagnation point, and as can be seen in Fig. 3.9, the variation of C_p away from the stagnation point closely follows a sine-squared behavior.

3.4 Centrifugal Force Corrections to Newtonian Theory

In the derivation of the straight Newtonian law, Eq. (3.3), we considered flow over a flat surface, such as the model sketched in Fig. 3.1. However, we proceeded to apply Eq. (3.3) to curved surfaces, such as in Figs. 3.4, 3.5, and 3.9. Is this theoretically consistent? The answer is no; for flow over a curved surface, there is a centrifugal force acting on the fluid elements, which will affect the pressure on the surface. For an application of Newtonian theory to curved surfaces that is totally consistent with theoretical mechanics, we must modify the discussion in Sec. 3.2 to take into account the centrifugal force effects. This is the purpose of the present section. Moreover, the results of this section are needed to support the discussion in the next section on the real meaning of Newtonian theory.

64 HYPersonic AND HIGH-TEMPERATURE GAS DYNAMICS

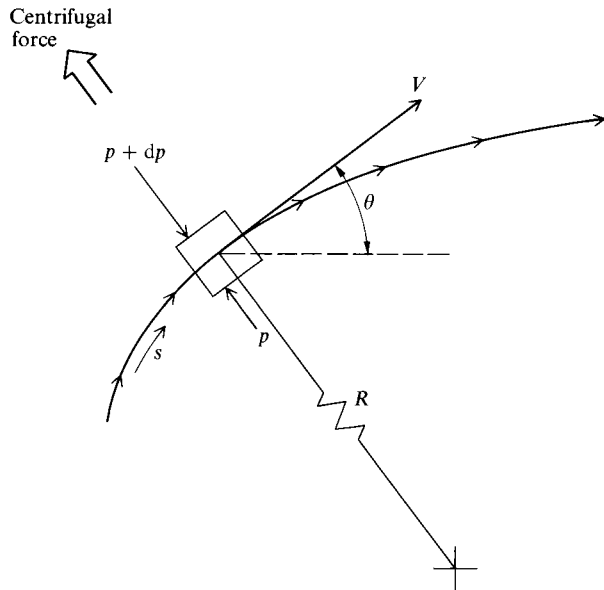


Fig. 3.10 Centrifugal force on a fluid element moving along a curved streamline.

To physically understand the nature of centrifugal force on a flowfield, consider a fluid element moving at velocity V along a curved streamline with radius of curvature R , as sketched in Fig. 3.10. The fluid element is experiencing a radial acceleration V^2/R with an attendant centrifugal force in the radial direction, as also shown in Fig. 3.10. To balance this centrifugal force and keep the fluid element moving along the streamline, the pressure $p + dp$ on the top surface of the element must be larger than the pressure p on the bottom surface, that is, there must be a positive pressure gradient in the radial direction. One could then theorize that, in the flow over a convex surface, the pressure would decrease in a normal direction toward the surface. This is a general fluid dynamic trend, not just limited to Newtonian theory. However, it is especially true for the mechanics associated with the Newtonian model. For flow over a convex surface, we should expect the Newtonian pressure to be *decreased* as a result of the centrifugal effect. This is derived as follows.

Consider Fig. 3.11, which illustrates the Newtonian flow over a curved surface. Consistent with the Newtonian model, all particles that impact the surface subsequently move tangentially over the surface in an infinitely thin layer. For the time being, assume this layer to have small thickness Δn ; later we will let $\Delta n \rightarrow 0$ consistent with the Newtonian approximation. Therefore, in Fig. 3.11 we are considering a thin layer of flow over the body, bounded by the dashed line and the body itself. (For clarity of presentation, the thickness of this layer is greatly magnified in Fig. 3.11.) Consider point i on the body surface. At point i we wish to calculate the pressure p_i . Through point i , consider

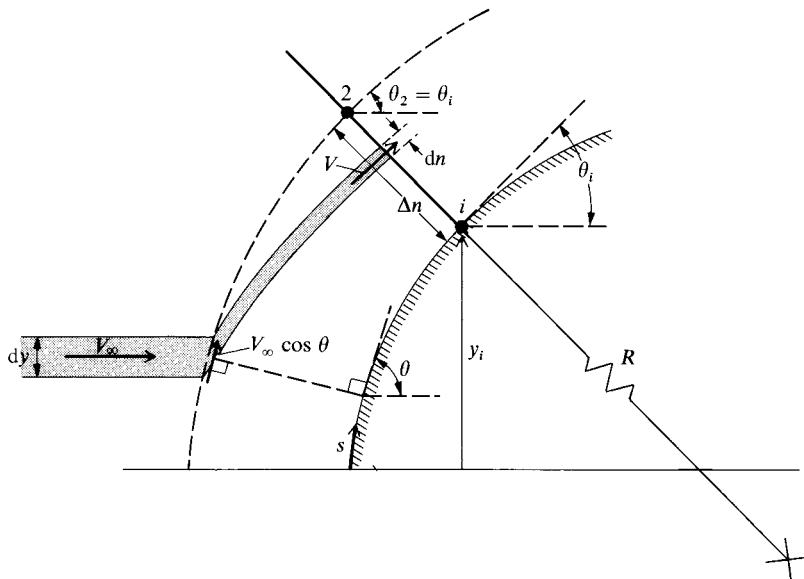


Fig. 3.11 Shock-layer model for centrifugal force corrections to Newtonian theory.

a streamline coordinate system, where s and n are coordinates locally tangential and perpendicular to the streamline. The radius of curvature of the streamline is R . The layer of flow over the body is so thin that we assume R is the same for all of the streamlines crossing the coordinate n drawn from point i over the distance Δn . As a result of this assumption, because the surface at point i is at the angle θ_i with respect to the freestream, then the angle at point 2 made by the outer edge of the layer (dashed line) with respect to the freestream is also θ_i . Now consider a streamtube within the layer, as shown by the shaded region in Fig. 3.11. In the freestream ahead of the layer, the height of this streamtube is dy , where y is the coordinate perpendicular to the freestream, and the velocity is V_∞ . Immediately upon entering the layer, the flow direction is assumed to be θ , the local deflection angle of the body at that location, and the magnitude of the velocity is $V_\infty \cos \theta$ —all consistent with the Newtonian model. Where the streamtube crosses the normal coordinate n drawn through point i , the thickness of the streamtube is dn , and the velocity is V . Concentrate on this part of the streamtube, that is, where it crosses n . At this location, Newton's second law written in streamline coordinates for the motion of a fluid element is, in the normal direction (for example, see [9]),

$$\frac{\partial p}{\partial n} = \frac{\rho V^2}{R} \quad (3.20)$$

Equation (3.20) states that the centrifugal force per unit volume of a fluid element $\rho V^2/R$ is exactly balanced by the normal pressure gradient $\partial p/\partial n$. Integrating

66 HYPersonic AND HIGH-TEMPERATURE GAS DYNAMICS

Eq. (3.20) across the layer from point i to point 2, we have

$$\int_{p_i}^{p_2} dp = \int_0^{\Delta n} \frac{\rho V^2}{R} dn \quad (3.21)$$

Assuming two-dimensional flow, the constant mass flow through the shaded streamtube dictates that

$$\rho_\infty V_\infty dy = pV dn \quad (3.22)$$

Substituting Eq. (3.22) into (3.21), we obtain

$$p_2 - p_i = \int_0^{y_i + \Delta n \cos \theta_i} \frac{\rho_\infty V_\infty}{R} V dy \quad (3.23)$$

where the direction of integration now becomes the vertical coordinate y . Note that the vertical coordinates of points i and 2 are y_i and $y_i + \Delta n \cos \theta_i$, respectively. Recall that dy in Eqs. (3.22) and (3.23) is the incremental height of the streamtube measured in the freestream and that all of the mass flow through the section of the layer of thickness Δn above point i originates in the total vertical extent of the freestream from the bottom line up to point 2. Hence, in Eq. (3.23) the limits of integration are taken from $y = 0$ to $y = y_i + \Delta n \cos \theta_i$. Making the assumption of an infinitesimally thin layer, we let $\Delta n \rightarrow 0$ or, more correctly, $y_i \gg \Delta n \cos \theta_i$. In this limit, Eq. (3.23) becomes

$$p_2 - p_i = \int_0^{y_i} \frac{\rho_\infty V_\infty}{R} V dy \quad (3.24)$$

We now make another assumption consistent with the Newtonian model. Because Newtonian theory assumes inelastic collisions of the particles with the surface wherein all of the normal momentum is lost but the tangential momentum is preserved, it is consistent to assume that the velocity of any given particle after collision is constant. Hence, in Fig. 3.11, we assume that the flow velocity along the shaded streamtube inside the layer is constant, that is, $V = V_\infty \cos \theta$ along the streamtube, including the section above point i . With this, and recalling that R is assumed constant for all streamlines crossing n above point i , Eq. (3.24) becomes

$$p_2 - p_i = \frac{\rho_\infty V_\infty^2}{R} \int_0^{y_i} \cos \theta dy \quad (3.25)$$

Recall from the definition of radius of curvature that, at point i ,

$$R = -\frac{1}{(d\theta/ds)_i} = -\frac{1}{(d\theta/dy)_i \sin \theta_i} \quad (3.26)$$

LOCAL SURFACE INCLINATION METHODS

67

Combining Eqs. (3.25) and (3.26) and rearranging, we have

$$p_i = p_2 + \rho_\infty V_\infty^2 \left(\frac{d\theta}{dy} \right)_i \sin \theta_i \int_0^{y_i} \cos \theta dy \quad (3.27)$$

Subtracting p_∞ from both sides of Eq. (3.27) and dividing by q_∞ , we obtain the pressure coefficient

$$C_{p_i} = C_{p_2} + 2 \left(\frac{d\theta}{dy} \right)_i \sin \theta_i \int_0^{y_i} \cos \theta dy \quad (3.28)$$

Finally, at point 2 the flow is just entering the layer and is being deflected through the angle θ_i ; there is no centrifugal effect at this point, and hence from Newtonian theory the pressure coefficient at point 2 must be interpreted as the straight Newtonian result given by Eq. (3.3), namely, $2 \sin^2 \theta_i$. With this, Eq. (3.28) is written as

$$C_{p_i} = 2 \sin^2 \theta_i + 2 \left(\frac{d\theta}{dy} \right)_i \sin \theta_i \int_0^{y_i} \cos \theta dy \quad (3.29)$$

Equation (3.29) is the Newtonian pressure coefficient at point i on a curved *two-dimensional* surface taking into account the centrifugal force correction. The first term on the right-hand side is the straight Newtonian result; the second term is the theoretically consistent correction for centrifugal effects. An analogous equation for *axisymmetric bodies* is

$$C_{p_i} = 2 \sin^2 \theta_i + 2 \left(\frac{d\theta}{dy} \right)_i \frac{\sin \theta_i}{y_i} \int_0^{y_i} y \cos \theta dy \quad (3.30)$$

Equation (3.30) can be written in terms of the local cross-sectional area $A = \pi y_2$.

$$C_{p_i} = 2 \sin^2 \theta_i + 2 \left(\frac{d\theta}{dA} \right)_i \sin \theta_i \int_0^{A_i} \cos \theta dA \quad (3.31)$$

The derivations of Eqs. (3.30) and (3.31) are left as homework problems.

The results embodied in Eqs. (3.29–3.31) were first obtained by Adolf Busemann in 1933 [10], with analogous approaches given in [11] and [12]. For this reason, Newtonian theory as modified for centrifugal force effects is frequently called *Newtonian–Busemann theory*.

Note from Eqs. (3.29–3.31) that Newtonian theory with the centrifugal modification is not totally a local surface inclination result. The value of C_{p_i} depends not only on the local inclination angle θ_i , but also on the shape of the body upstream of point i through the presence of the integral terms. In some sense, this is compatible with the true physical nature of steady supersonic and hypersonic flows where conditions at a given point are influenced by pressure

68 HYPersonic AND HIGH-TEMPERATURE GAS DYNAMICS

waves from the upstream region but not from the downstream region. (Recall that information cannot propagate upstream in steady supersonic flow.) However, do not be misled; this aspect of Newtonian–Busemann theory has nothing to do with the true physical picture of the propagation of information via pressure waves—indeed, such propagation is not a part of the Newtonian model. Rather, the integral terms in Eqs. (3.29–3.31) are simply expressions associated with the *mass flow* through the layer immediately above point i in Fig. 3.11. This mass flow depends on the velocity profile along n , $V = V(n)$. In the Newtonian model shown in Fig. 3.11, recall that we assumed that the flow velocity is constant along a streamline inside the layer, and hence the value of V at a given n depends on the location (hence the local value of θ) where the streamline first enters the layer. This is how the dependence of C_{pi} on the shape of the body upstream of point i enters the formulation.

Equations (3.29) and (3.30) take on a particularly simple form for *slender bodies*, where θ is small. For small θ ,

$$\begin{aligned}\sin \theta_i &\rightarrow \theta_i \\ \int_0^{y_i} \cos \theta \, dy &\rightarrow y_i\end{aligned}$$

Also, letting ds be an incremental length along the surface, $dy = \sin \theta \, ds$, and hence $\sin \theta_i (d\theta/dy)_i = (d\theta/ds)_i = \kappa_i$, where κ_i is the *curvature* of the surface at point i . Thus, Eqs. (3.29) and (3.30) become (dropping the subscript)

$$C_p = 2(\theta^2 + \kappa y): \text{for slender 2-D bodies} \quad (3.32a)$$

$$C_p = 2\theta^2 + \kappa y: \text{for slender bodies of revolution} \quad (3.32b)$$

For flow over a blunt body, the centrifugal correction actually makes things worse. For example, Fig. 3.12 shows predictions for the pressure coefficient over a circular cylinder based on all three types of Newtonian-like flow: Newtonian, modified Newtonian, and Newtonian–Busemann. These results are compared with an exact numerical calculation carried out by Van Dyke for $M_\infty = \infty$ (see [14]). Note from Fig. 3.12 that Newtonian theory gives the correct qualitative variation, but is off by a constant percentage, and that modified Newtonian is quite accurate. However, the Newtonian–Busemann results are neither qualitatively nor quantitatively correct. A similar trend occurs for slender-body cases as shown in Fig. 3.13. Here, the pressure distribution over a 10% thick biconvex airfoil is predicted by both Newtonian and Newtonian–Busemann theories and compared with exact numerical results from the method of characteristics. For $\gamma = 1.4$, the Newtonian–Busemann is again worse than straight Newtonian. In Fig. 3.13, the method-of-characteristic results are obtained from [15], and the Newtonian results from [13] and [16].

LOCAL SURFACE INCLINATION METHODS

69

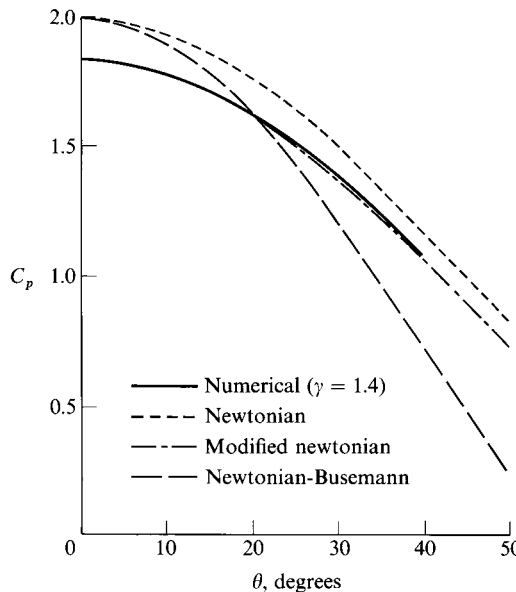


Fig. 3.12 Surface-pressure distributions for flow past a circular cylinder: $M_\infty = \infty$ and $\gamma = 1.4$ (from [13]).

In light of the results shown in Figs. 3.12 and 3.13, we conclude that the centrifugal force correction to Newtonian theory, although correct from the point of view of theoretical mechanics, is simply not valid for practical applications. For this reason, the centrifugal force corrections are rarely, if ever, seen in contemporary applications of Newtonian theory for hypersonic vehicle

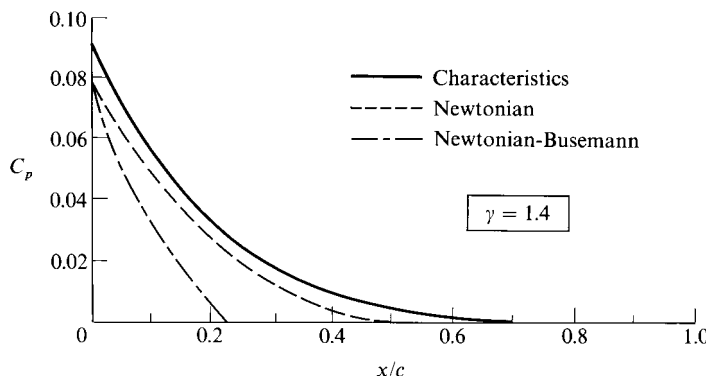


Fig. 3.13 Surface-pressure distribution over a 10% thick biconvex airfoil. Shape of the airfoil is shown in Fig. 3.14: $M_\infty = \infty$, and $\gamma = 1.4$ (from [15]).

70 HYPersonic AND HIGH-TEMPERATURE GAS DYNAMICS

design. Therefore, why have we spent an entire section of this book discussing such corrections? Is it only an academic exercise, at best? The answer is—not quite. This is the subject of the next section.

3.5 Newtonian Theory—What It Really Means

In Secs. 3.2–3.4, the theoretical basis of Newtonian theory was developed, including the centrifugal force effects. Given the Newtonian flow model, Eq. (3.3) for a flat surface and Eqs. (3.29) and (3.30) for curved surfaces are precise results, obtained by the rigorous application of theoretical mechanics to the postulated model. On the other hand, when we apply Newtonian theory to practical hypersonic flow problems in air we have seen in Secs. 3.3 and 3.4 that the best agreement with exact results is obtained *without* the centrifugal force corrections, which at first glance appears theoretically inconsistent. Indeed, straight Newtonian theory [Eq. (3.3), or Lee's modification given by Eq. (3.15)] frequently gives very acceptable results for pressure distributions over hypersonic bodies in air, whether or not these bodies have straight or curved surfaces. Therefore, is Newtonian theory just an approximation that fortuitously gives reasonable results for hypersonic flow? Is the frequently obtained good agreement between Newtonian and exact results just a fluke? The answer is *no*—Newtonian theory has true physical significance if, in addition to considering the limit of $M_\infty \rightarrow \infty$, we also consider the limit of $\gamma \rightarrow 1.0$. Let us examine this in more detail.

Temporarily discard any thoughts of Newtonian theory, and simply recall the exact oblique shock relation for C_p as given by Eq. (2.14), repeated next (with freestream conditions now denoted by a subscript ∞ rather than a subscript 1, as used in Chapter 2):

$$C_p = \frac{4}{\gamma + 1} \left(\sin^2 \beta - \frac{1}{M_\infty^2} \right) \quad (2.14)$$

Equation (2.15) gave the limiting value of C_p as $M_\infty \rightarrow \infty$ repeated here.

As $M_\infty \rightarrow \infty$:

$$C_p \rightarrow \frac{4}{\gamma + 1} \sin^2 \beta \quad (2.15)$$

Now take the additional limit of $\gamma \rightarrow 1.0$. From Eq. (2.15), in both limits as $M_\infty \rightarrow \infty$ and $\gamma \rightarrow 1.0$, we have

$$C_p \rightarrow 2 \sin^2 \beta \quad (3.33)$$

Equation (3.33) is a result from exact oblique shock theory; it has nothing to do with Newtonian theory (as yet). Keep in mind that β in Eq. (3.33) is the wave angle, not the deflection angle.

LOCAL SURFACE INCLINATION METHODS

71

Let us go further. Consider the exact oblique shock relation for ρ_2/ρ_∞ , given by Eq. (2.3) repeated here (again with subscript ∞ replacing the subscript 1):

$$\frac{\rho_2}{\rho_\infty} = \frac{(\gamma + 1)M_\infty^2 \sin^2 \beta}{(\gamma - 1)M_\infty^2 \sin^2 \beta + 2} \quad (2.3)$$

Equation (2.4) was obtained as the limit where $M_\infty \rightarrow \infty$, namely
As $M_\infty \rightarrow \infty$:

$$\frac{\rho_2}{\rho_\infty} \rightarrow \frac{\gamma + 1}{\gamma - 1} \quad (2.4)$$

In the additional limit as $\gamma \rightarrow 1$, we find that

As $\gamma \rightarrow 1$ and $M_\infty \rightarrow \infty$:

$$\frac{\rho_2}{\rho_\infty} \rightarrow \infty$$

(3.34)

That is, the density behind the shock is *infinitely large*. In turn, mass flow consideration then dictate that the *shock wave is coincident with the body surface*. This is further substantiated by Eq. (2.19), which is good for $M_\infty \rightarrow \infty$ and small deflection angles

$$\frac{\beta}{\theta} \rightarrow \frac{\gamma + 1}{2} \quad (2.19)$$

In the additional limit as $\gamma \rightarrow 1$, we have

As $\gamma \rightarrow 1$ and $M_\infty \rightarrow \infty$ and θ and β small:

$$\beta = \theta$$

That is, the shock wave lies on the body. In light of this result, Eq. (3.33) is written as

$$C_p = 2 \sin^2 \theta$$

(3.35)

Examine Eq. (3.35). It is a result from exact oblique shock theory, taken in the combined limit of $M_\infty \rightarrow \infty$ and $\gamma \rightarrow 1$. However, it is also precisely the Newtonian result given by Eq. (3.3). Therefore, we make the following conclusion. The closer the actual hypersonic flow problem is to the limits $M_\infty \rightarrow \infty$ and $\gamma \rightarrow 1$, the closer it should be described physically by Newtonian

72 HYPersonic AND HIGH-TEMPERATURE GAS DYNAMICS

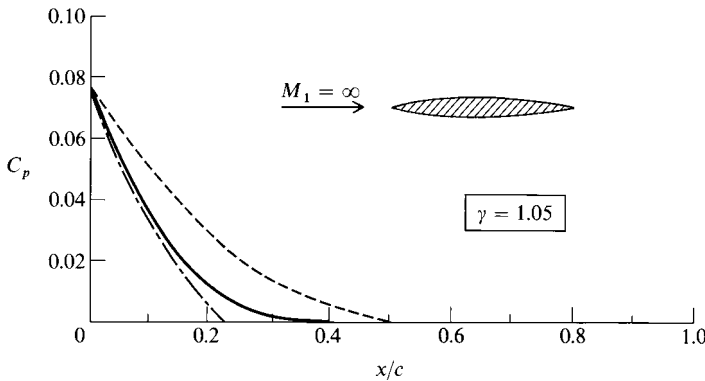


Fig. 3.14 Same as Fig. 3.13, except with $\gamma = 1.05$ (from [15]).

flow. Also in this combined limit, the centrifugal correction becomes physically appropriate, and the Newtonian–Busemann theory gives better results than straight Newtonian. For example, Fig. 3.14 illustrates the pressure coefficient over a 10% thick biconvex airfoil at $M_\infty = \infty$; this is the same type of comparison made in Fig. 3.13. However, Fig. 3.14 is for $\gamma = 1.05$, and clearly the Newtonian–Busemann theory gives much closer agreement with the exact method of characteristics than does the straight Newtonian. This is in direct contrast with the results for $\gamma = 1.4$, shown in Fig. 3.13. Therefore, we conclude that the application of Newtonian theory to hypersonic flow has some direct theoretical substance, becoming more accurate as $\gamma \rightarrow 1$. Furthermore, for hypersonic flows in air with $\gamma = 1.4$, we would not expect the full Newtonian theory (properly including centrifugal effects) to be accurate, and, as we have seen in Figs. 3.12 and 3.13, it is not. On the other hand, for air with $\gamma = 1.4$, agreement between exact results and the straight Newtonian theory (without centrifugal effects) does indeed appear to be rather fortuitous.

We might ask the rather academic question: if in the limit of $M_\infty \rightarrow \infty$ and $\gamma \rightarrow 1$, the shock-layer thickness goes to zero, then how can there be any centrifugal force felt over this zero thickness? The answer is, of course, that in the same limit the density becomes infinite, and although the shock layer approaches zero thickness, the infinite density felt over this zero thickness is an indeterminate form that yields a finite centrifugal force.

As a final note on our discussion of Newtonian theory, consider Fig. 3.15. Here, the pressure coefficients for a 15-deg half-angle wedge and a 15-deg half-angle cone are plotted vs freestream Mach number for $\gamma = 1.4$. The exact wedge results are obtained from oblique shock theory, and the exact cone results are obtained from the solution of the classical Taylor–MacColl equation (for example, see [4]) as tabulated in [17] and [18]. Both sets of results are compared with Newtonian theory, $C_p = 2 \sin^2 \theta$, shown as the dashed line in Fig. 3.14. This comparison demonstrates two general aspects of Newtonian results:

- 1) The accuracy of Newtonian results improves as M_∞ increases. This is to be expected from our preceding discussion. Note from Fig. 3.15 that below

LOCAL SURFACE INCLINATION METHODS

73

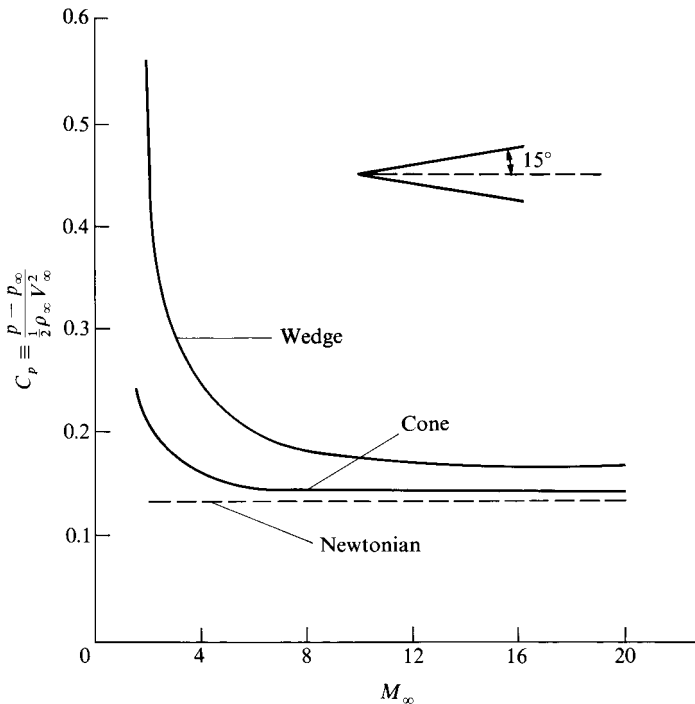


Fig. 3.15 Comparison between Newtonian and exact results for the pressure coefficient on a sharp wedge and a sharp cone.

$M_\infty = 5$ the Newtonian results are not even close, but the comparison becomes much closer as M_∞ increases above 5.

2) **Newtonian theory is usually more accurate for three-dimensional bodies** (e.g., the cone) **than for two-dimensional bodies** (e.g., the wedge). This is clearly evident in Fig. 3.15, where the Newtonian result is much closer to the cone results than to the wedge results.

These two trends are general conclusions that seem to apply to Newtonian results for hypersonic bodies in air. Furthermore, we are tempted to say that Newtonian results for blunt bodies should use the modified Newtonian formula [Eq. (3.15)], and that such results usually produce acceptable accuracy, as illustrated in Figs. 3.9 and 3.12. In contrast, we suggest that Newtonian results for slender bodies should use the straight Newtonian law [Eq. (3.3)], and we observe that its accuracy might not be totally acceptable in some cases. For example, for Fig. 3.15, at $M_\infty = 20$, the percentage error in using Newtonian results is 19 and 5% for the wedge and cone, respectively—not as accurate as might be required for some applications. If the modified Newtonian formula [Eq. (3.15)] had been used in Fig. 3.15, the errors would be even larger because $C_{p,\max} < 2$. Therefore, we conclude that although Newtonian theory is very useful because of its simplicity, in some applications its accuracy leaves something to be desired.

74 HYPersonic AND HIGH-TEMPERATURE GAS DYNAMICS

As a parenthetical comment, Fig. 3.15 illustrates another trend that is characteristic of hypersonic flow. Note that, at low M_∞ the exact values of C_p for both the wedge and cone decrease rapidly with increasing Mach number. However, at higher values of M_∞ the pressure coefficient for each shape tends to seek a plateau, approaching a value that becomes rather independent of M_∞ at high Mach number. This is an example of the Mach-number independence principle, to be discussed in Chapter 4. There we will see that a number of properties in hypersonic flow, including C_p , lift coefficient, wave-drag coefficient, and moment coefficient become relatively independent of M_∞ at high Mach number.

3.5.1 Worked Example: Comparison of Newtonian with Exact Theory

The purpose of this worked example is to provide even better insight into the advantages and disadvantages of Newtonian theory, especially as applied to slender bodies at small angles of attack. Vehicles designed for efficient hypersonic flight for sustained periods of time in the atmosphere will most likely be slender shapes at small angles of attack. Is Newtonian theory a reasonable method for estimating the pressure distribution on such vehicles? Let us take a look by considering the most slender of vehicles, namely, a thin flat plate, at a moderate angle of attack.

Consider an infinitely thin flat plate at an angle of attack of 15 deg in a Mach 8 flow. Assume inviscid flow. Calculate the pressure coefficients on the top and bottom surface of the plate, the lift and drag coefficients, and the lift-to-drag ratio using a) exact shock-wave and expansion-wave theory and b) Newtonian theory. Compare the results.

Solution: exact theory. Consider the flat plate shown in Fig. 3.16. The flow over the top goes through an expansion wave, and the flow over the bottom goes through an oblique shock wave. First, consider the flow through the expansion wave. Using the terminology in Fig. 2.4, $M_1 = 8$, and from Eq. (2.32), the Prandtl–Meyer function is $\nu_1 = 95.62$ deg. From Eq. (2.31),

$$\nu_2 = \theta + \nu_1 = 15 \text{ deg} + 95.62 \text{ deg} = 110.62 \text{ deg}$$

With $\nu_2 = 110.62$ deg, Eq. (2.32) yields for M_2 ,

$$M_2 = 14.32$$

The flow through an expansion wave is isentropic; hence, the total pressure is constant through the wave. Let p_o denote the total pressure. Because the total pressure is constant,

$$p_{o2} = p_{o1}$$

LOCAL SURFACE INCLINATION METHODS

75

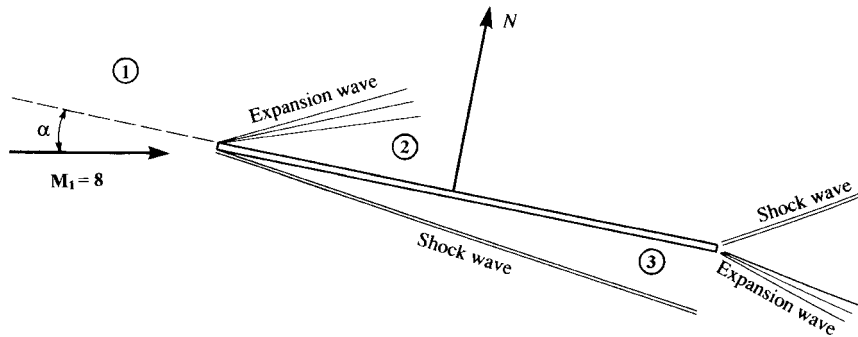


Fig. 3.16 Wave system on a flat plate in hypersonic flow.

and we can write the static-pressure ratio across the expansion wave as

$$\frac{p_2}{p_1} = \frac{p_{o1}/p_1}{p_{o2}/p_2}$$

For a calorically perfect gas, the ratio of total to static pressure at a point in the flow is a function of the local Mach number at that point (for example, see [4] and [5]), given by

$$\frac{p_o}{p} = \left[1 + \frac{\gamma - 1}{2} M^2 \right]^{\frac{\gamma}{\gamma-1}}$$

Hence,

$$\frac{p_2}{p_1} = \frac{p_{o1}/p_1}{p_{o2}/p_2} = \left[\frac{1 + (\gamma - 1/2)M_1^2}{1 + (\gamma - 1/2)M_2^2} \right]^{\frac{\gamma}{\gamma-1}}$$

With $M_1 = 8$ and $M_2 = 14.32$, this gives

$$\frac{p_2}{p_1} = 0.0203$$

The pressure coefficient is given by Eq. (2.13)

$$C_{p_2} = \frac{2}{\gamma M_1^2} \left(\frac{p_2}{p_1} - 1 \right)$$

76 HYPersonic AND HIGH-TEMPERATURE GAS DYNAMICS

Hence,

$$C_{p_2} = \frac{2}{(1.4)(8)^2} (0.0203 - 1) = \boxed{-0.0219}$$

To obtain the pressure coefficient on the bottom surface from oblique shock theory, Eq. (2.16) with $\theta = 15$ deg and $M_1 = 8$ yields a shock-wave angle of $\beta = 21$ deg. From Eq. (2.1) with $\beta = 21$ deg and $M_1 = 8$, and denoting the pressure behind the shock as p_3 consistent with Fig. 3.16, we have

$$\frac{p_3}{p_1} = 9.443$$

Hence, the pressure coefficient on the bottom surface is

$$C_{p_3} = \frac{2}{\gamma M_1^2} \left(\frac{p_3}{p_1} - 1 \right)$$

$$C_{p_3} = \frac{2}{(1.4)(8)^2} (9.443 - 1) = \boxed{0.1885}$$

From Eq. (3.8), the normal-force coefficient is simply

$$c_n = C_{p_3} - C_{p_2} = 0.1885 - (-0.0219) = 0.2104$$

From Eq. (3.10)

$$c_\ell = c_n \cos \alpha = 0.2104 \cos 15 \text{ deg} = \boxed{0.2032}$$

and from Eq. (3.11),

$$c_d = c_n \sin \alpha = 0.2104 \sin 15 \text{ deg} = \boxed{0.0545}$$

Finally,

$$\frac{L}{D} = \frac{c_\ell}{c_d} = \frac{0.2032}{0.0545} = \boxed{3.73}$$

Note: For more details on how to make these exact shock-wave and expansion-wave calculations, for example, see [4] and [5]. As a case in point, in the preceding calculations, Eq. (2.16) was used to find the shock-wave angle, $\beta = 21$ deg. To do this arithmetically, Eq. (2.16) would have to be solved by trial and error. In reality, the value $\beta = 21$ deg was obtained from a graphical plot of Eq. (2.16) called the θ - β - M curves, as explained in [4] and [5].

LOCAL SURFACE INCLINATION METHODS

77

Solution: Newtonian theory. From Eq. (3.7) for the upper surface of the plate,

$$C_{p_2} = 0$$

From Eq. (3.6) for the lower surface of the plate,

$$C_{p_3} = 2 \sin^2 \alpha = 2 \sin^2 15 \text{ deg} = [0.134]$$

From Eq. (3.12)

$$c_\ell = 2 \sin^2 \alpha \cos \alpha = 2(\sin^2 15 \text{ deg})(\cos 15 \text{ deg}) = [0.1294]$$

and from Eq. (3.13),

$$c_d = 2 \sin^3 \alpha = 2 \sin^3 15 \text{ deg} = [0.03468]$$

Finally,

$$\frac{L}{D} = \frac{c_\ell}{c_d} = \frac{0.1294}{0.03468} = [3.73]$$

3.5.2 Commentary

The preceding example provides some important comparisons between exact theory and Newtonian theory. First, compare the work effort to obtain the answers. Going through the exact calculations was much more work than using the simple Newtonian theory. Indeed, the Newtonian calculations were essentially “one-liners” to get the answers—nothing could be more simple. This comparison highlights the value of Newtonian theory—absolute simplicity. But this simplicity is obtained at a cost, namely, a loss of accuracy. For example, for the pressure coefficient on the bottom surface of the plate, we have the following.

Exact:

$$C_{p_3} = 0.1885$$

Newtonian:

$$C_{p_3} = 0.134$$

Newtonian theory *underpredicts* the pressure coefficient on the lower surface by 29%. For the top surface of the plate, we have the following.

Exact:

$$C_{p_2} = -0.0219$$

78 HYPersonic AND HIGH-TEMPERATURE GAS DYNAMICS

Newtonian:

$$C_{p_2} = 0$$

Newtonian theory *overpredicts* the pressure coefficient on the upper surface by a 100% of the exact value. For the lift coefficient, we have the following.

Exact:

$$c_\ell = 0.2032$$

Newtonian:

$$c_\ell = 0.1294$$

For the drag coefficient, we have the following.

Exact:

$$c_d = 0.0545$$

Newtonian:

$$c_d = 0.03468$$

The Newtonian results underpredict both c_ℓ and c_d by 36%. However, the values of L/D ratio compare exactly.

Exact:

$$\frac{L}{D} = 3.73$$

Newtonian:

$$\frac{L}{D} = 3.73$$

This is no surprise, for two reasons. First, the Newtonian values of c_ℓ and c_d are both underpredicted by the same percentage; hence, their ratio is not affected. Second, the value of L/D for inviscid flow over a flat plate, no matter what theory is used to obtain the pressures on the top and bottom surfaces, is simply a matter of *geometry* as discussed earlier in conjunction with Eq. (3.14). From this equation,

$$\frac{L}{D} = \cot \alpha = \cot 15 \text{ deg} = 3.73$$

A conclusion from the preceding example as well as from the comparison shown in Fig. 3.15 is that Newtonian theory when applied to hypersonic slender bodies at small to moderate angles of attack does not do a good job of

estimating surface pressure or the resulting lift and wave drag. Newtonian theory is much more applicable to hypersonic blunt bodies; the Newtonian pressure distribution around the nose of a blunt body is reasonably accurate as illustrated in Fig. 3.9.

3.5.3 Lift-to-Drag Ratio for Hypersonic Bodies—Comment

The magnitude of the lift-to-drag ratio calculated in the preceding example is important to note—it is very low in comparison to those values for a flat plate in subsonic or even supersonic flow. Here is a harbinger of things to come. Hypersonic flight vehicles suffer from characteristically low values of L/D . This is not good news when designing hypersonic vehicles for sustained flight in the atmosphere. The lift-to-drag ratio of a body is a direct measure of its aerodynamic efficiency (for example, see [1]). For example, everything else being equal, the higher is the value of L/D , the larger is the range of the vehicle. The design of hypersonic vehicles with reasonable values of L/D is a challenge and a quest, as will be discussed later in this book.

3.6 Tangent-Wedge Tangent-Cone Methods

Referring again to the road map given in Fig. 1.24, we remind ourselves that we are discussing a class of hypersonic prediction methods based only on a knowledge of the local surface inclination relative to the freestream. The Newtonian theory discussed in Secs. 3.2–3.5 was one such example; the tangent-wedge/tangent-cone methods presented in this section are two others.

Let us consider first the tangent-wedge method, applicable to two-dimensional hypersonic shapes. Consider the two-dimensional body shown as the hatched area in Fig. 3.17. Assume that the nose of the body is pointed and that the

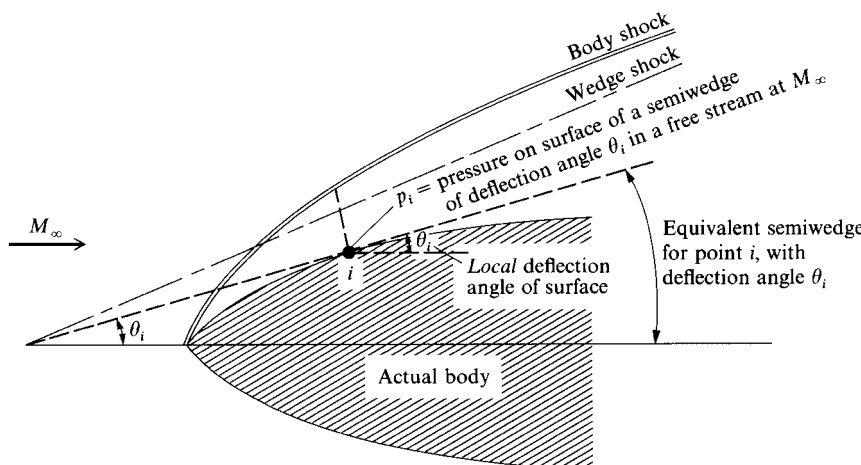


Fig. 3.17 Illustration of the tangent-wedge method.

80 HYPersonic AND HIGH-TEMPERATURE GAS DYNAMICS

local surface inclination angle θ at all points along the surface is less than the maximum deflection angle for the freestream Mach number. Consider point i on the surface of the body; we wish to calculate the pressure at point i . The local deflection angle at point i is θ_i . Imagine a line drawn tangent to the body at point i ; this line makes an angle θ_i with respect to the freestream and can be imagined as the surface of an equivalent wedge with a half-angle of θ_i , as shown by the dashed line in Fig. 3.17. The tangent-wedge approximation assumes that the pressure at point i is the same as the surface pressure on the equivalent wedge at the freestream Mach number M_∞ , that is, p_i is obtained directly from the exact oblique shock relations for a deflection angle of θ_i and a Mach number of M_∞ .

The tangent-cone method for application to axisymmetric bodies is analogous to the tangent-wedge method and is illustrated in Fig. 3.18. Consider point i on the body: a line drawn tangent to this point makes the angle θ_i with respect to the freestream. Shown as the dashed line in Fig. 3.18, this tangent line can be imagined as the surface of an equivalent cone, with a semiangle of θ_i . The tangent-cone approximation assumes that the pressure at point i is the same as the surface pressure on the equivalent cone at a Mach number of M_∞ , that is, p_i is obtained directly from the cone tables such as [17] and [18].

Both the tangent-wedge and tangent-cone methods are very straightforward. However, they are approximate methods, not based on any theoretical grounds. We cannot “derive” these methods from a model of the flow to which basic mechanical principles are applied, in contrast to the theoretical basis for Newtonian flow. Nevertheless, the tangent-wedge and tangent-cone methods frequently yield reasonable results at hypersonic speeds. Why? We can give an approximate, “hand-waving” explanation, as follows. First, consider a line drawn perpendicular to the body surface at point i , across the shock layer as sketched in Fig. 3.17. Note that the imaginary shock wave from the imaginary equivalent wedge crosses this line below the point where the actual shock wave from the body

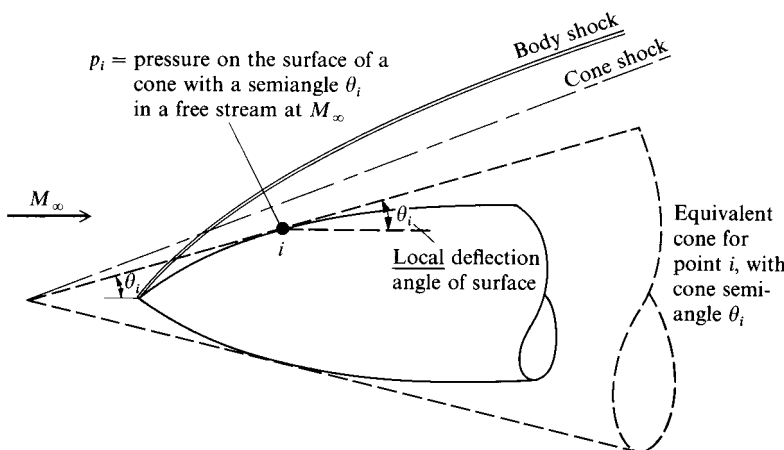


Fig. 3.18 Illustration of the tangent-cone method.

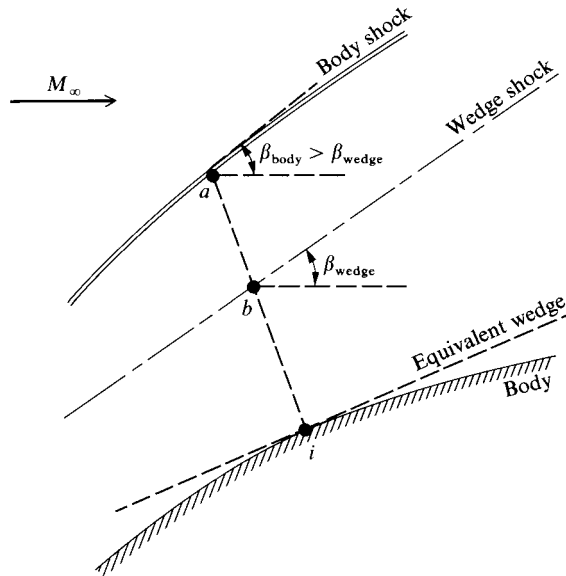


Fig. 3.19 Segment of a hypersonic shock layer, for use in partial justification of the tangent-wedge method.

crosses the line. The region around this line is isolated and magnified in Fig. 3.19. Now consider the following fact.

Fact: In the hypersonic flow across an oblique shock wave on a slender body, the y component of the flow velocity v is changed much more strongly than the x component u .

This fact, which we will revisit several times in the following chapters, is proved by a combination of Eqs. (2.7), (2.10), and (2.19), which yields in the limit of $M_\infty \rightarrow \infty$ (referring to the shock geometry shown in Fig. 2.2)

$$\frac{\Delta u}{V_\infty} = \frac{V_\infty - u_2}{V_\infty} \rightarrow \frac{\gamma + 1}{2} \theta^2 \quad (3.36)$$

$$\frac{\Delta v}{V_\infty} = \frac{v_2}{V_\infty} \rightarrow \theta \quad (3.37)$$

In Eq. (3.36), Δu is the change in the x component of velocity across the oblique shock, and in Eq. (3.37) Δv is the change in the y component of velocity. Clearly, the change of the v velocity is considerably *smaller* (order of θ^2) than the change of the u velocity (order of θ). (Keep in mind that θ is a small angle in radians.) In turn, recalling Euler's equation $dp = -\rho V dV$, this implies that the major pressure gradients are *normal to the flow*. Referring to Fig. 3.19, the principal change in pressure is therefore along the normal line iab ; by comparison,

82 HYPersonic AND HIGH-TEMPERATURE GAS DYNAMICS

changes in the flow direction are second order. Hence examining Fig. 3.19, the surface pressure on the body at point i is *dominated by the pressure behind the shock at point a* . Because of the centrifugal force effects, the pressure at point i , p_i , will be *less than p_a* . Now, in the tangent-wedge method $p_i = p_b$, where p_b is the pressure behind the imaginary wedge shock (at point b in Fig. 3.19). The pressure p_b is already less than p_a because the imaginary wedge shock angle at point b is less than the actual body-shock angle at point a ($\beta_{\text{body}} > \beta_{\text{wedge}}$). Thus we see that the wedge pressure p_b is a reasonable approximation for the surface pressure p_i because in the real flow picture the higher pressure p_a behind the body shock is mitigated by centrifugal effects as the pressure is impressed from the shock to the body at point i . The same reasoning holds for the tangent-cone method.

Results obtained with the tangent-cone method as applied to a pointed ogive are shown in Fig. 3.20, taken from [19]. Here, the surface-pressure distribution is plotted vs distance along the ogive. Four sets of results are presented, each for a different value of $K = M_\infty (d/l)$, where d/l is the slenderness ratio of the ogive. The solid line is an exact result obtained from the rotational method of characteristics, and the dashed line is the tangent-cone result. Very reasonable agreement is obtained, thus illustrating the usefulness of the tangent-cone method, albeit its rather tenuous foundations. The same type of agreement is typical of the tangent-wedge method. In Fig. 3.20, the parameter $K = M_\infty (d/l)$ is called the hypersonic similarity parameter. Its appearance in Fig. 3.20 is simply a precursor to our discussion of hypersonic similarity in Chapter 4.

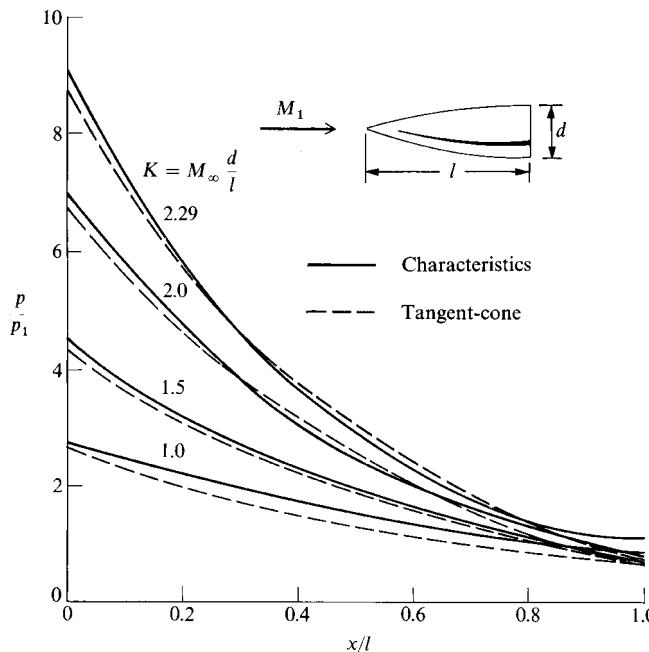


Fig. 3.20 Surface-pressure distributions for ogives of different slenderness ratio d/l (from [19]).

3.7 Shock-Expansion Method

Of the local surface inclination methods discussed so far, the Newtonian method can be applied to a body surface of any inclination angle, whereas the tangent-wedge/tangent-cone methods require a local surface angle less than the shock detachment angle for the given freestream Mach number. This is why Newtonian theory can be applied to blunt-nosed bodies, but the tangent-wedge/tangent-cone methods are limited to sharp-nosed bodies with attached shock waves. The method discussed in the present section—the shock-expansion method—is in the latter category. It assumes a sharp-nosed body with an attached shock wave. However, it has more theoretical justification than the tangent-wedge/tangent-cone methods, as described next.

Consider the hypersonic flow over a sharp-nosed two-dimensional body with an attached shock wave at the nose as sketched in Fig. 3.21. The deflection angle at the nose is θ_n . The essence of the shock-expansion theory is as follows:

- 1) Assume the nose is a wedge with semiangle θ_n . Calculate M_n and p_n behind the oblique shock at the nose by means of exact oblique-shock theory.
- 2) Assume a local Prandtl–Meyer expansion along the surface downstream of the nose. We wish to calculate the pressure at point i , p_i . To do this, we must first obtain the local Mach number at point i , M_i . This is obtained from the Prandtl–Meyer function, assuming an expansion through the deflection angle $\Delta\theta = \theta_n - \theta_i$.

$$\Delta\theta = \sqrt{\frac{\gamma+1}{\gamma-1}} \tan^{-1} \sqrt{\frac{\gamma-1}{\gamma+1} (M_n^2 - 1)} - \tan^{-1} \sqrt{\frac{\gamma-1}{\gamma+1} (M_i^2 - 1)} - \left[\tan^{-1} \sqrt{M_n^2 - 1} - \tan^{-1} \sqrt{M_i^2 - 1} \right] \quad (3.38)$$

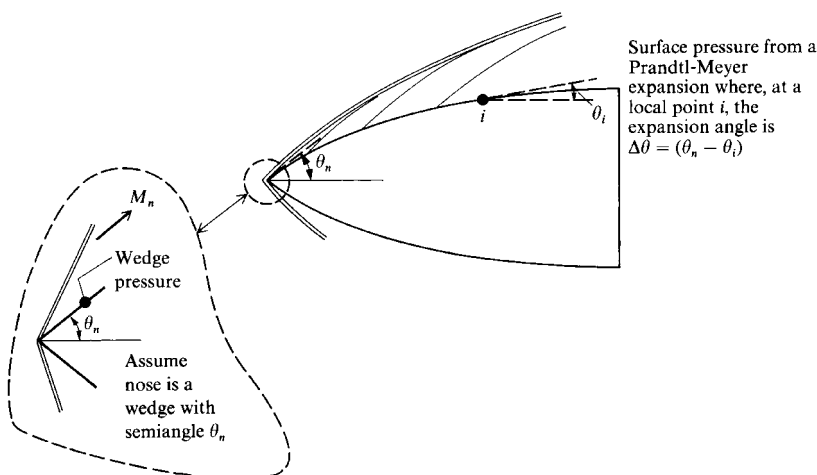


Fig. 3.21 Illustration of the shock-expansion method.

84 HYPersonic AND HIGH-TEMPERATURE GAS DYNAMICS

In Eq. (3.38), M_i is the only unknown; M_n is known from the preceding step 1, and $\Delta\theta = \theta_n - \theta_i$ is a known geometric quantity. Of course, for air with $\gamma = 1.4$ tables for the Prandtl–Meyer function abound (for example, see [4]), and in such a case the tables would be used to calculate M_i rather than attempting to solve Eq. (3.38) implicitly for M_i .

- 3) Calculate p_i from the isentropic flow relation

$$\frac{p_i}{p_n} = \left[\frac{1 + (\gamma - 1)/2M_n^2}{1 + (\gamma - 1)/2M_i^2} \right]^{\gamma/(\gamma-1)} \quad (3.39)$$

(Again, for air with $\gamma = 1.4$, the isentropic flow tables, such as found in [4], can be used to obtain p_i in a more convenient manner.)

Results from the shock-expansion method, obtained from [20] for flow over a 10%-thick biconvex airfoil are shown in Fig. 3.22, as compared with the exact method of characteristics. Excellent agreement is obtained. This is to be somewhat expected. After passing through the attached shock wave at the nose, the actual flow does indeed expand around the body, and this expansion process is approximated by the assumption of a local Prandtl–Meyer expansion. Why this is not a precisely exact calculation is discussed two paragraphs below.

The shock-expansion method can also be applied to bodies of revolution. The method is essentially the same as shown in Fig. 3.21, except now θ_n is assumed to be the semiangle of a cone, and M_n and p_n at the nose are obtained from the exact Taylor–MacColl cone results. Then the Prandtl–Meyer expansion relations are applied locally downstream of the nose. This implies that the flow downstream of the nose is locally two dimensional, which assumes that the divergence of streamlines in planes tangential to the surface. For bodies of revolution at zero degree angle of attack, this condition is usually met. Results for the shock-expansion method applied to ogives at zero angle of attack are shown in

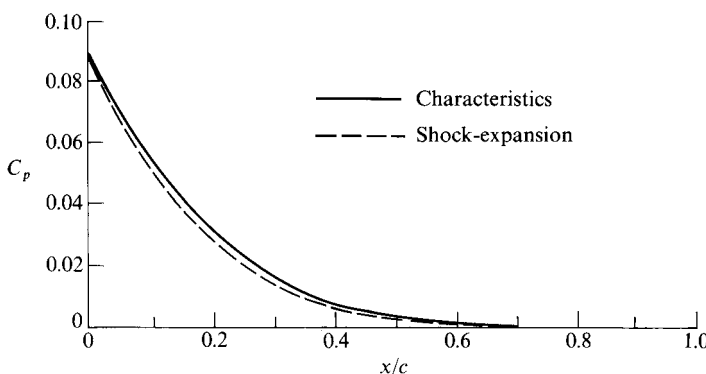


Fig. 3.22 Surface-pressure distribution over the same 10%-thick airfoil as shown in Fig. 3.14; comparison of the shock-expansion method with exact results from the method of characteristics: $M_\infty = \infty$ (from [20]).

LOCAL SURFACE INCLINATION METHODS

85

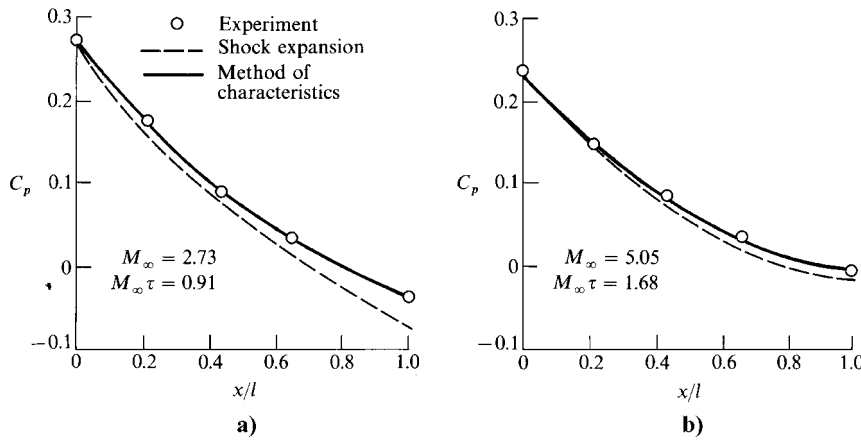


Fig. 3.23 Pressure distribution over an ogive with $d/l = 1/3$ at zero angle of attack with $\gamma = 1.4$ (from [21]): a) supersonic case and b) hypersonic case.

Fig. 3.23, obtained from [21]. The ogive has a slenderness ratio $d/l = 1/3$. In Fig. 3.23a, the results are for a supersonic Mach number $M_\infty = 2.73$, whereas in Fig. 3.23b, the results are for a slightly hypersonic case $M_\infty = 5.05$. The circles are experimental data, the solid line represents an exact result from the method of characteristics, and the dashed line is from the shock-expansion method. Note that, for the supersonic case the shock-expansion method yields poor agreement; however, for the hypersonic case the shock-expansion method is much closer to the hypersonic case, and the shock-expansion method is much closer to the exact result. There is a reason for this, as explained in the following.

Consider Fig. 3.24, which contains schematics of supersonic and hypersonic flows over a pointed body with an attached shock wave. Downstream of the

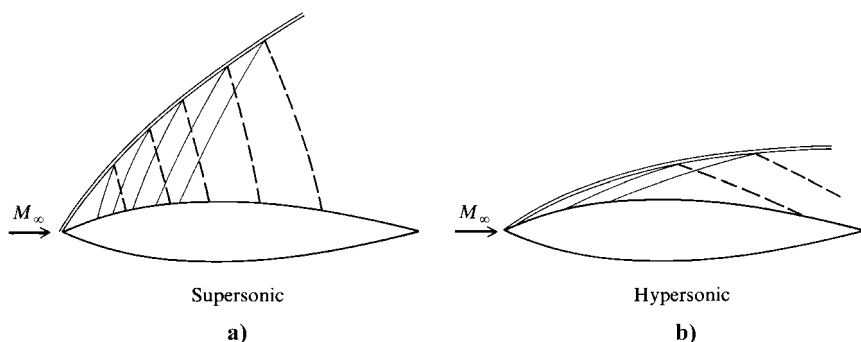


Fig. 3.24 Schematic of shock-wave and Mach-wave patterns: a) supersonic and b) hypersonic.

86 HYPersonic AND HIGH-TEMPERATURE GAS DYNAMICS

shock wave, expansion waves are generated at the surface of the body and propagate outward, eventually intersecting the bow shock wave. These expansion waves reflect from the shock wave; the reflected waves propagate back to the body surface, as shown by the dashed lines in Fig. 3.24. *Shock-expansion theory ignores the effect of these reflected waves on the body surface pressure.* Now consider just the supersonic case sketched in Fig. 3.24a. At supersonic Mach numbers, the shock angles and the incident and reflected wave angles are large. [The incident and reflected waves are essentially Mach waves with the Mach angle $\mu = \arcsin(1/M)$, where M is the local Mach number; at low Mach number, μ is large.] As a result, as seen in Fig. 3.24a, the reflected waves influence a considerable portion of the body surface, and this influence is not taken into account by the shock-expansion method. In contrast, for the hypersonic case shown in Fig. 3.24b, the shock and Mach angles are much smaller, and the reflected waves propagate much further downstream before they hit the body surface. As a result the reflected waves do not greatly influence the surface pressure, especially on the forward portion of the body. Therefore, the real hypersonic picture satisfies the assumption of shock-expansion theory more closely than the supersonic picture, and it is no surprise that shock-expansion theory yields better agreement at higher Mach numbers.

3.8 Summary and Comments

This chapter has dealt with hypersonic local surface inclination methods—such methods predict the local surface pressure as a function of the local surface inclination angle relative to the freestream direction θ . The methods discussed were 1) the straight Newtonian method, which yields

$$C_p = 2 \sin^2 \theta \quad (3.3)$$

2) the modified Newtonian method, which states

$$C_p = C_{p_{\max}} \sin^2 \theta \quad (3.15)$$

3) the Newton–Busemann method, which takes into account the centrifugal force correction. For a two-dimensional body, this result is

$$C_{p_i} = 2 \sin^2 \theta_i + 2 \left[\frac{d\theta}{dy} \right]_i \sin \theta_i \int_0^{y_i} \cos \theta \, dy \quad (3.29)$$

4) the tangent-wedge method, where the pressure at point i on a two-dimensional body is assumed to be the same as a wedge with deflection angle θ_i ; 5) the tangent-cone method, where the pressure at point i on an axisymmetric body is assumed to be the same as a cone with the semicone angle of θ_i ; and 6) the shock-expansion method, where the pressure distribution downstream of the attached shock wave on a two- or three-dimensional body is assumed to be given by a local Prandtl–Meyer expansion. It is not possible to state with any certainty which of the preceding methods is the best for a given application. All of these

methods have their strengths and weaknesses, and some intuitive logic is required to choose one over the others for a given problem. For example, in the prediction of the pressure distribution over a hypersonic airplane any distinguishable portions of the fuselage might be treated with the tangent-cone method, whereas the wings might be better treated with the tangent-wedge method. Of course, for surfaces with large inclination angles (greater than the maximum deflection angle for an oblique shock wave at the given M_∞) the Newtonian method is appropriate. Within the confines of the Newtonian method itself, for blunt surfaces, where θ is very large, modified Newtonian is best, whereas straight Newtonian usually yields better results for slender bodies. In both cases, for $\gamma = 1.4$ the centrifugal force correction leads to poor results and should not be used. (Keep in mind that although the centrifugal force correction is theoretically consistent with mechanical principles, it is quantitatively correct only in the combined limit of $M_\infty \rightarrow \infty$ and $\gamma \rightarrow 1$.)

In regard to all of the local surface inclination methods discussed here, none of the preceding judgments on accuracy and applicability are totally definitive, and they all must be taken in the spirit of suggestions only. However, one definitive statement can be made about all of these methods, namely, that they are straightforward and easy to apply. For this reason, they are popular design tools for the investigation of large numbers of different hypersonic bodies. Indeed, *all* of the local surface inclination methods discussed in this chapter are embodied in an industry-standard computer program called the "Hypersonic Arbitrary Body Program" originally prepared by Gentry [22], and for this reason frequently referred to as the "Gentry program." This program has been in wide use throughout industry and government since the early 1970s. All of these methods discussed in this chapter are options within the Gentry program, which can be called at will for application to different portions of a hypersonic body. This program, and modified versions of it, is widely used in the preliminary design and analysis of hypersonic vehicles. It is mentioned here only to reinforce the engineering practicality of the methods discussed in this chapter.

Design Example 3.1

This is the first of a number of design examples in this book. The main thrust of this book is to present the *fundamental* aspects of hypersonic and high-temperature gas dynamics. We will from time to time, however, seize the moment to elaborate on the design applications of the fundamentals. This is such a moment.

The Hypersonic Arbitrary Body program (HABP), an elaborate computer program for predicting the surface-pressure, shear-stress, and heat-transfer distributions over hypersonic bodies of arbitrary shape, as well as their lift, drag, and moment coefficients, uses the local surface inclination methods discussed in this chapter. In fact, HABP offers a choice of 17 different pressure-prediction methods, but the primary ones of choice are Newtonian, modified Newtonian, tangent wedge, tangent cone, and shock expansion—all discussed in this chapter. The methods used for the prediction of shear stress and heat transfer are discussed

88 HYPersonic AND HIGH-TEMPERATURE GAS DYNAMICS

in Chapter 6. The purpose of HABP is to provide an easy-to-use, fast, and reliable hypersonic aerodynamic prediction code for use in the preliminary design of hypersonic vehicles. Developed by the Douglas Aircraft Company in 1964, the code was greatly expanded in 1973, and then further updated in 1980. As mentioned earlier, this code is frequently referred to as the Gentry program after one of its originators [22]. The HABP is still in use today as a preliminary design tool.

An interesting and completely independent evaluation of HABP was made by Carren M. E. Fisher of British Aerospace P.L.C. In [225], Fisher presents calculations made with the Mark IV version of HABP for a variety of different vehicle configurations for which experimental data exist. In HABP, the vehicle surface is divided into a large number of flat surfaces (panels). For example, Fig. 3.25 shows the paneling used to represent the geometry of the space shuttle. Knowing the freestream Mach number and the angle of inclination of each panel relative to the freestream, a chosen local surface inclination method is used to obtain the pressure coefficient on each panel. Table 3.1, from [225], lists the available methods that can be chosen; there is a list for the windward side of the vehicle and a separate list for the leeward side.

Consider the tangent ogive-cylinder boattail shape given at the top of Fig. 3.26. Shown below the vehicle shape are results for the normal-force coefficient C_N , center-of-pressure location X_{cp} , moment coefficient about the nose C_m , and the axial-force coefficient C_A , respectively, as a function of angle of attack for a freestream Mach number of 4.63. The solid triangles are experimental data from Landrum ([226]). These data are compared with results from HABP using four different pressure-prediction methods labeled according to the numbering in Table 3.1. The curve labeled 1,1 ($K = 2.0$) pertains to item 1, modified Newtonian, for the windward side and item 1, Newtonian (i.e., $C_p = 0$), on the leeward side; K is the modified Newtonian correction factor, given by

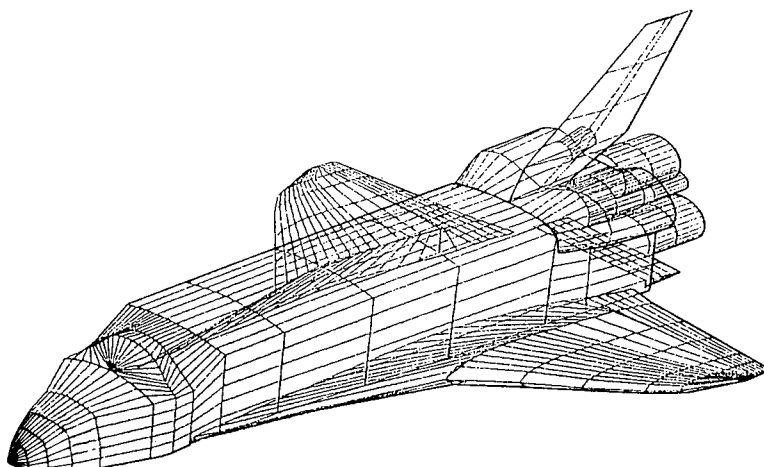


Fig. 3.25 Panel distribution over the space shuttle for an HAPB calculation (from Fisher [225]).

LOCAL SURFACE INCLINATION METHODS

89

Table 3.1 List of options in HAPB^a

Method no.	Impact method (applied to windward side of vehicle)	Shadow method (applied to leeward side of vehicle)
1	Modified Newtonian	Newtonian (i.e., $C_p = 0$)
2	Modified Newtonian and Prandtl–Meyer	Modified Newtonian and Prandtl–Meyer
3	Tangent-wedge (Using oblique shock)	Prandtl–Meyer expansion
4	Tangent-wedge empirical	Inclined-cone
5	Tanget-cone	Van Dyke unified
6	Inclined-cone	High Mach number base pressure ($C_p = -1/M^2$)
7	Van Dyke unified	Shock-expansion (using Strip theory)— Prandtl–Meyer expansion from freestream on first element of each stream-wise strip
8	Blunt-body skin-friction Shear-force	Input pressure coefficient
9	Shock-expansion (using Strip theory)	Free molecular flow
10	Free-molecular flow	Mirror Dahlem–Buck
11	Input pressure coefficient	ACM Empirical data
12	Hankey flat-surface Empirical	OSU Blunt body empirical
13	Delta-wing empirical	
14	Dahlem–Buck empirical	
15	Blast-wave pressure increments	
16	Modified tangent cone	
17	OSU Blunt body empirical	

^aImpact methods 16 and 17 and shadow methods 10, 11, and 12 are recent updates to S/HAPB.

$C_p = K \sin^2 \theta$. Here, $K = 2.0$; hence, $C_p = 2 \sin^2 \theta$, which is really the straight Newtonian results. The curve labeled 1,1 ($K = 1.81$) is the same set of methods except with a different value of K , where $C_p = 1.81 \sin^2 \theta$. The curve labeled 14, 1 uses the Dahlem–Buck empirical method (not described in this chapter) for the windward side and the Newtonian ($C_p = 0$) for the leeward side. And finally the fourth curve uses 6,4, inclined cone, for both the windward and leeward sides of the ogive portion of the vehicle, and 3,2 ($K = 1.81$), tangent wedge for the windward side and a combination of modified Newtonian with $K = 1.81$ and Prandtl–Meyer for the leeward side of the cylinder-boattail portion. Comparing the results shown in Fig. 3.26, this fourth curve gives

90 HYPersonic AND HIGH-TEMPERATURE GAS DYNAMICS

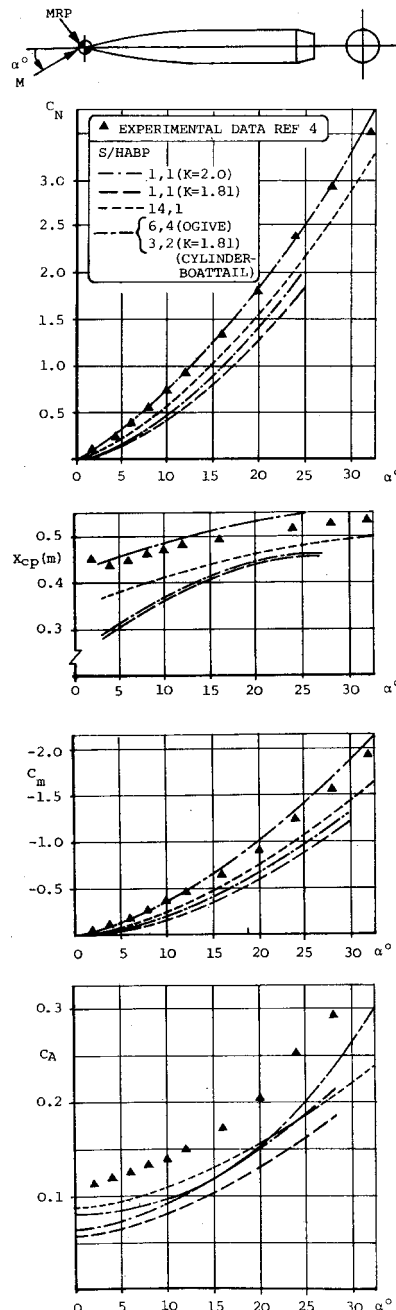


Fig. 3.26 Aerodynamic coefficients for a tangent ogive-cylinder boat-tail configuration, where $M_\infty = 4.63$ (from Fisher [225]).

LOCAL SURFACE INCLINATION METHODS

91

the best agreement with experiment, illustrating the value of mixing and matching various options available in HABP for different parts of the vehicle. The normal-force coefficient C_N is accurately predicted, and the location of the center-of-pressure X_{cp} and the moment coefficient about the nose C_m are reasonably predicted. All of the pressure prediction methods underpredict the axial-force coefficient C_A because skin friction is not included in these particular results. Also, keep in mind that the results shown in Fig. 3.26 are for $M_\infty = 4.63$, a relatively low Mach number for applicability of the local surface inclination methods discussed in this chapter.

Return to Fig. 3.25, which shows the panel distribution for a space shuttle calculation. Predicted aerodynamic data for the space shuttle at Mach 13.5 obtained from HABP are compared with wind tunnel and flight data in Fig. 3.27. The predictions from HABP use only one combination, 1,1 ($K = 2.0$), that is, straight Newtonian. The wind-tunnel and flight data are from [227]. Figure 3.27 gives the variations of C_N , C_A , C_m , C_D , C_L , and L/D as functions of angle of attack. The wind-tunnel data span the complete angle-of-attack interval, whereas only one flight data point is shown on each graph because Mach 13.5 pertains to a specific point on the entry flight path, hence to only one specific space shuttle angle of attack. For the most part, the HABP calculations are markably close to the wind-tunnel data over the range of angle of attack. The flight data, given here from STS-1, for some of the coefficients deviate slightly from both the wind-tunnel data and the HABP calculations. But on the whole, we can see that HABP is a useful engineering prediction code for the space shuttle aerodynamics.

This statement is reinforced by the data shown in Fig. 3.28. Here the lift, drag, and moment coefficients, and the lift-to-drag ratio, for the space shuttle are given as a function of Mach number as the shuttle flies down its entry flight path. The flight data from STS-5 are given by the circles, and the preflight predictions from [227] are given by the triangles. Calculations using four different methods from HABP are also shown in Fig. 3.28. The discontinuities shown here are caused by shuttle maneuvers, which are not accounted for in the calculations. The two HABP methods labeled "with shielding" refer to the shielding option in HABP, which accounts for the reduction in pressure on an elemental panel that is shielded (hidden) from the freestream flow by another panel; for such shielded panels the pressure coefficient is set to zero. Clearly, from the results shown in Fig. 3.28 HABP gives a reasonable prediction of the space shuttle aerodynamic characteristics with the exception of the moment coefficient. The discrepancy in the moment coefficient calculations is caused by flowfield chemically reacting effects not included in HABP (and not reflected in the NASA preflight prediction data, which are largely based on cold-flow hypersonic wind-tunnel tests); at the end of Sec. 14.9, this matter is discussed at length, and the effect of chemically reacting flow on the moment coefficient is shown.

Very recently, Kinney [228] at the NASA Ames Research Center developed a new aerodynamic prediction code labeled CBAERO, the Configuration Based Aerodynamic software package, much in the same spirit as the earlier HABP. This new code makes pressure predictions using the modified Newtonian, tangent-wedge, and tangent-cone methods discussed in this chapter. In contrast to HABP, however, CBAERO uses panels on the body surface that are an unstructured mesh of triangles, such as shown in Fig. 3.29 for the surface of

92 HYPersonic AND HIGH-TEMPERATURE GAS DYNAMICS

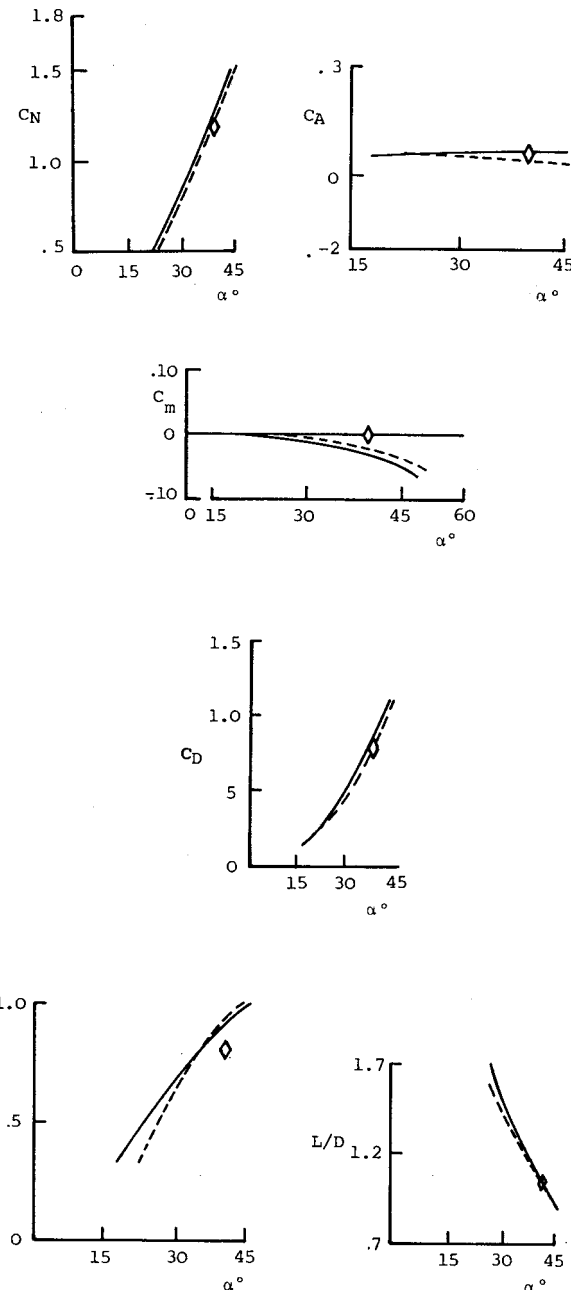


Fig. 3.27 Aerodynamic coefficient predictions using Newtonian theory, where $M_\infty = 13.5$ (from Fisher [225]).

LOCAL SURFACE INCLINATION METHODS

93

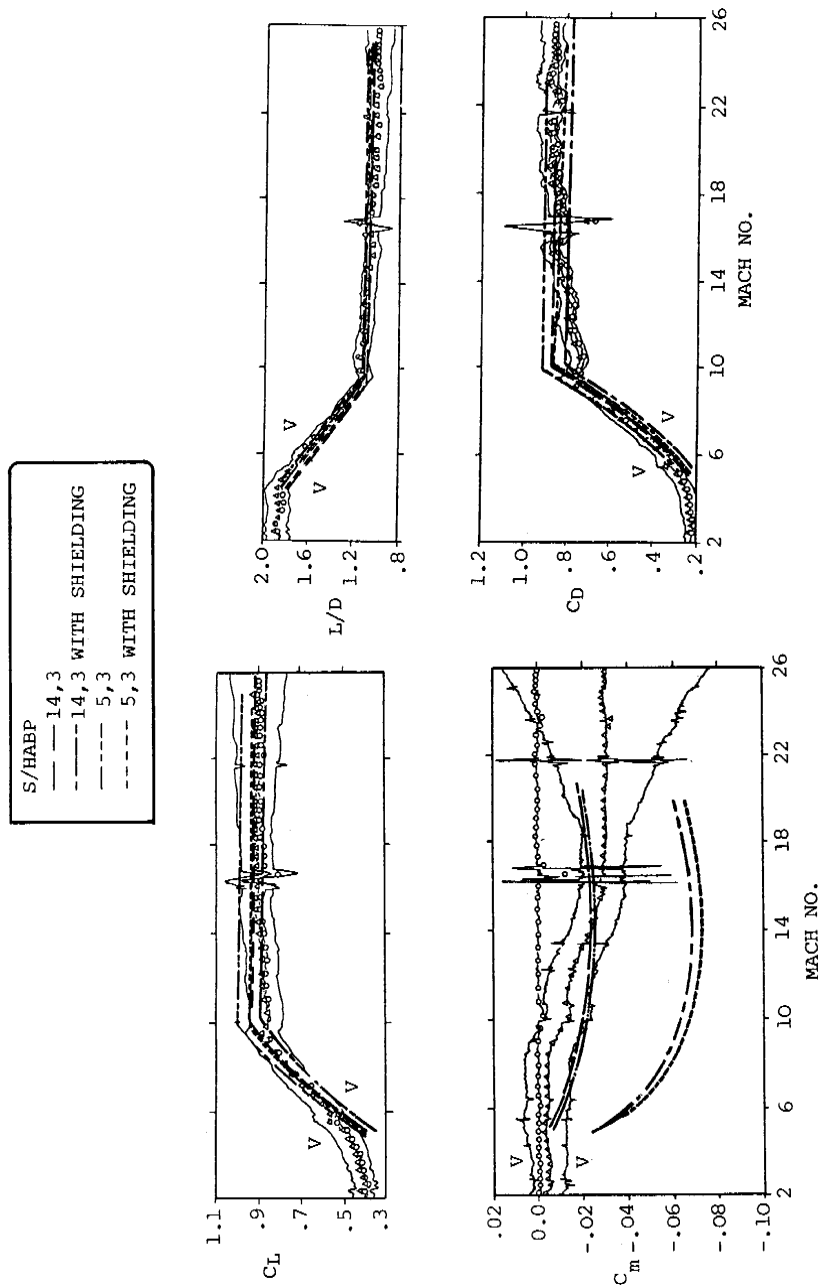


Fig. 3.28 STS-5 lift, drag, and moment variations during atmospheric entry. Predictions from HABP compared with flight data (from Fisher [225]).

94 HYPersonic AND HIGH-TEMPERATURE GAS DYNAMICS

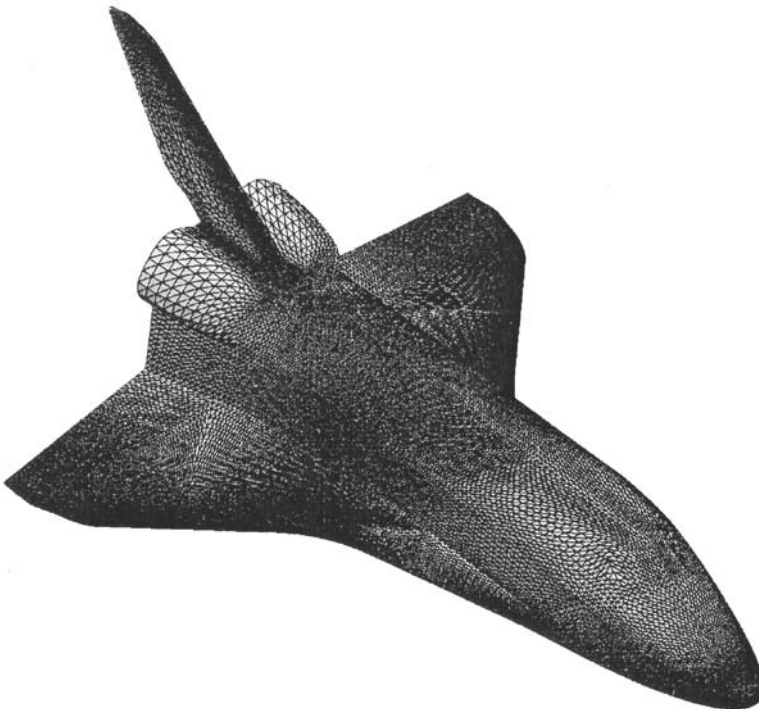


Fig. 3.29 Unstructured triangulated surface for the space shuttle (from Kinney and Garcia [229]).

the space shuttle. Compared to rectangular panels, this surface grid of triangles allows a more precise definition of complex vehicle geometries. Moreover, existing unstructured mesh-generation programs developed for use in computational fluid dynamics (CFD) can be used here for the body surface paneling. Indeed, this allows CBAERO results to be compared more directly with CFD results using the same mesh. In Fig. 3.29, the shuttle surface is covered by 103,104 triangles. Other modern features contained in CBAERO are the inclusion of high-temperature equilibrium chemically reacting flow thermodynamics (discussed in Chapter 14), the engineering prediction method of Tauber as well as the reference temperature method (discussed in Chapter 6) for convective aerodynamic heating, and an engineering method for stagnation radiative heat transfer (discussed in Chapter 18). This allows the use of CBAERO to predict the surface pressure, surface shear stress, convective heating, and radiative heating for vehicles operating in the severe aerothermal environments associated with flight Mach numbers as high as 36—that associated with Apollo-like atmospheric entries for a lunar mission.

Kinney and Garcia [229] computed surface pressures along the top and bottom centerlines of the space shuttle at Mach 24.87 and at angle of attack of 40.17 deg, as given in Fig. 3.30. Two sets of results are shown, one obtained from CBAERO and the other from a detailed CFD flowfield solution using a NASA Ames

LOCAL SURFACE INCLINATION METHODS

95

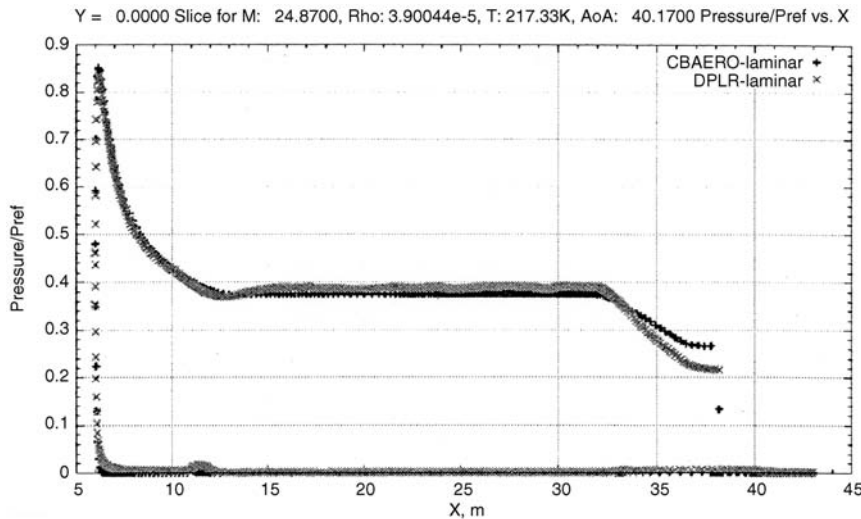


Fig. 3.30 Centerline pressure distribution for the space shuttle, where $M_\infty = 24.87$ and angle of attack 40 deg [229].

Research Center code labeled DPLR. The DPLR computational-fluid-dynamic results are the reference standard against which the CBAERO results are compared. The local surface inclination pressure prediction methods in CBAERO agree very well with the CFD results for both the windward surface (the upper curves) and the leeward surface (the lower curves).

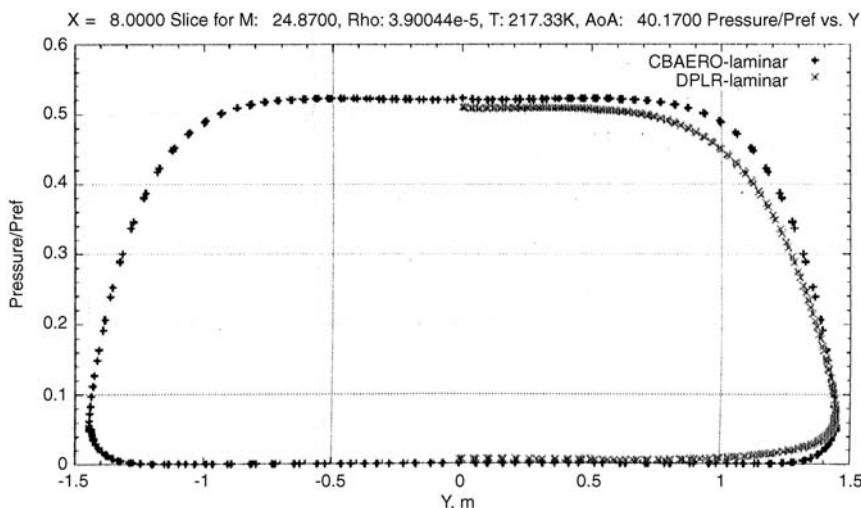


Fig. 3.31 Lateral pressure distribution for the space shuttle, where $M_\infty = 24.87$ and angle of attack 40 deg [229].

96 HYPersonic AND HIGH-TEMPERATURE GAS DYNAMICS

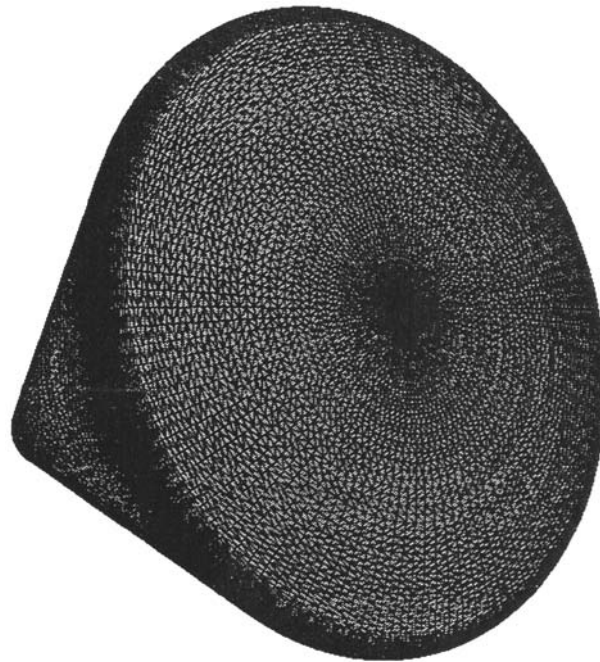


Fig. 3.32 Apollo command module with surface triangulation for CBAERO [229].

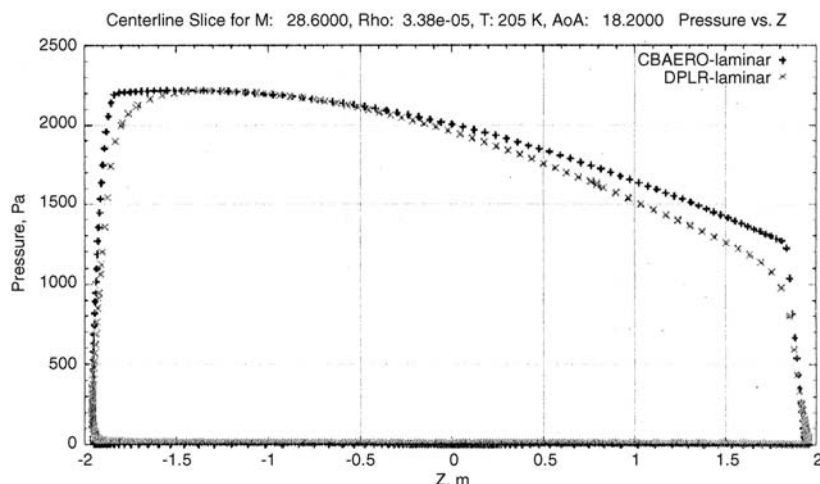


Fig. 3.33 Centerline pressure distribution for the Apollo command module, where $M_{\infty} = 28.6$ and angle of attack 18.2 deg [229].

LOCAL SURFACE INCLINATION METHODS

97

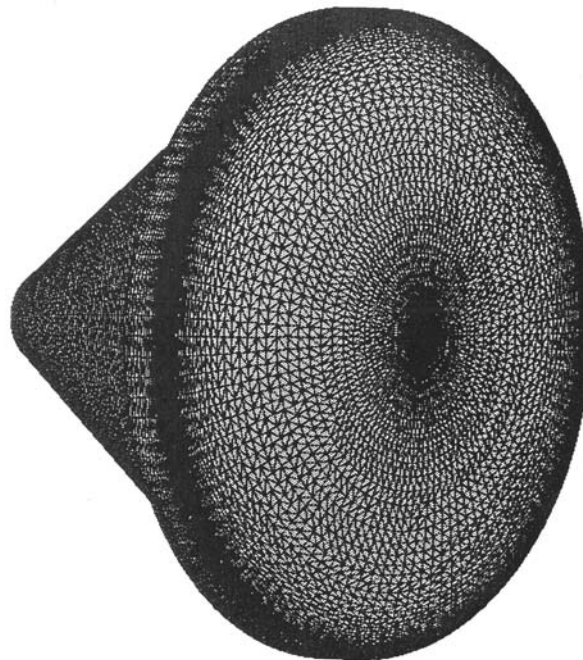


Fig. 3.34 Fire II test vehicle with surface triangulation for CBAERO [229].

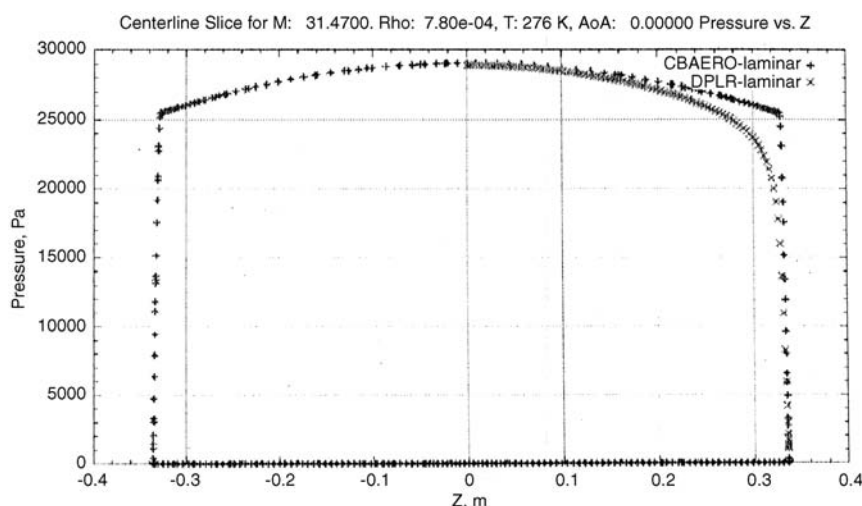


Fig. 3.35 Centerline pressure distribution for the Project Fire II test vehicle, where $M_{\infty} = 35.75$ and angle of attack 47 deg [229].

98 HYPersonic AND HIGH-TEMPERATURE GAS DYNAMICS

The lateral pressure distributions over the perimeter of a cross section of the space shuttle body are given in Fig. 3.31. The body cross section is located 8 m downstream of the nose. The pressure distribution is plotted vs the lateral coordinate y and forms a looped curve because at any given lateral location y there is a surface point on the windward side and another on the leeward side. The upper part of the loop (the higher pressures) corresponds to the windward side, and the lower part of the loop (the lower pressures) corresponds to the leeward side. Here we see that CBAERO slightly overpredicts the peak pressures on the windward side, especially along that side portion of the body with large lateral curvature, where three-dimensional flow effects are stronger.

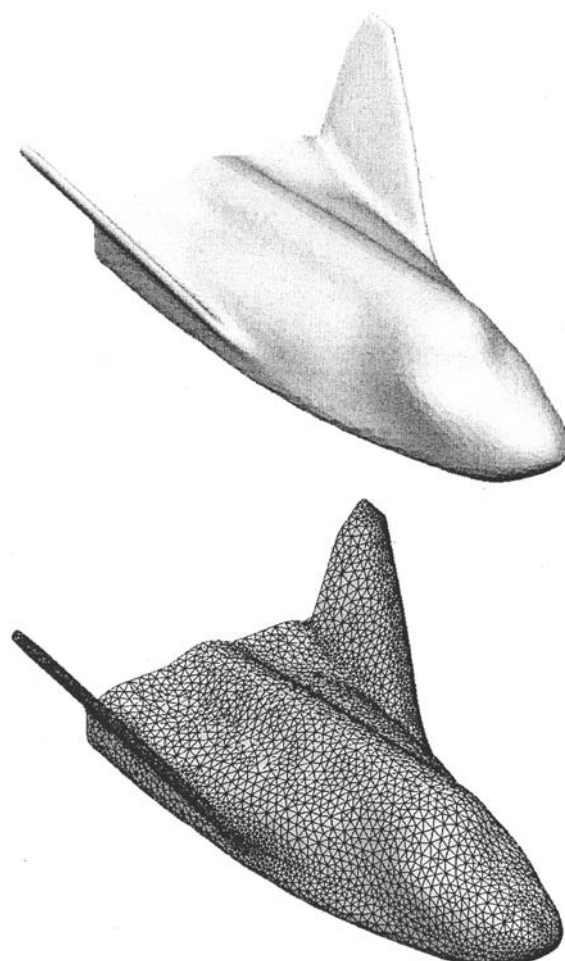


Fig. 3.36 HL-20 starting geometry and mesh for the optimization process using CBAERO (from Kinney [230]).

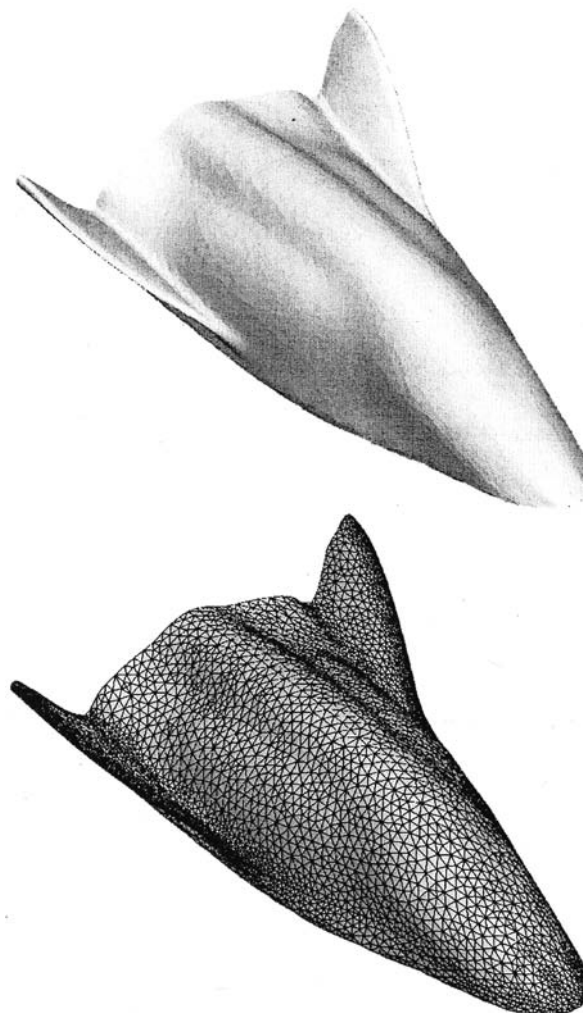


Fig. 3.37 Final optimized geometry and mesh after 100 design iterations using CBAERO [230].

Results obtained in a more severe aerothermal environment are given for the Apollo command module in Figs. 3.32 and 3.33. Figure 3.32 illustrates the triangular panel distribution over the surface of the module; here 29,000 triangles are used. The calculated centerline pressure distribution for the module at Mach 28.6, and an angle of attack of 18.2 deg is shown in Fig. 3.33, with results from CBAERO compared with the CFD results. In general, CBAERO does a reasonable job of predicting the Apollo Command Module pressure distribution.

Results obtained for an even more severe aerothermal environment are given for the Project Fire II test vehicle in Figs. 3.34 and 3.35. Figure 3.34 illustrates the

100 HYPersonic AND HIGH-TEMPERATURE GAS DYNAMICS

triangular panel distribution over the vehicle surface; here 25,800 triangles are used. The calculated centerline pressure distribution for the test vehicle at Mach 35.75 and an angle of attack of 47 deg is shown in Fig. 3.35, with results from CBAERO compared with the CFD results. The CBAERO results compare very well with the detailed CFD calculations except in the shoulder region, where CBAERO slightly overpredicts the pressure.

We end this Design Example with an example of CBAERO used for the optimized design of hypersonic vehicles. This example is taken from the work of Kinney as described in [230]. Starting with the HL-20 crew transfer vehicle shown in Fig. 3.36 at Mach 20 and an angle of attack of 20 deg as a baseline, Kinney obtained the optimized shape shown in Fig. 3.37 at the same Mach number and angle of attack. An angle of attack 20 deg was chosen because the baseline HL-20 has a maximum value of L/D of 1.514 at this angle of attack. The objective of the optimization is to maximum L/D while holding the volume of the vehicle constant and constraining the pitching moment to zero. The optimized shape in Fig. 3.37 has $L/D = 2.78$, almost twice that of the baseline vehicle. Recall that in the optimization procedure the angle of attack is held constant at 20 deg. Interestingly enough, Kinney found that the resulting optimized shape in Fig. 3.37 actually has a *maximum* $L/D = 3.24$ and that it occurs at an angle of attack near 15 deg. Comparing the optimized shape in Fig. 3.37 with the baseline HL-20 in Fig. 3.36, Kinney observed that the optimization process drove the optimized geometry towards a wedge-like configuration on the forward portion of the body and that the windward side of the vehicle took on a waverider-like shape. (Waveriders are discussed in Chapters 5 and 6.) He also noted that the fins took on a smooth dihedral shape and were reduced in size.

In conclusion, at the time of writing the local surface inclination methods discussed in this chapter, although developed for hypersonic applications in the 1950s, are certainly alive and well today. Indeed, they are the basis of the modern Configuration Based Aerodynamics prediction code (CBAERO) highlighted here, as well as the well-established Hypersonic Arbitrary Body program (HABP) discussed earlier.

Problems

- 3.1** Consider the variation of lift with angle of attack for an infinitely thin flat plate. Using Newtonian theory, prove that maximum lift occurs at $\alpha = 54.7$ deg.
- 3.2** From Newtonian theory, prove that the drag coefficient for a circular cylinder of infinite span is $4/3$.
- 3.3** From Newtonian theory, prove that the drag coefficient for a sphere is 1.
- 3.4** In problems 3.1–3.3, are the results changed by using *modified* Newtonian theory? Explain.

LOCAL SURFACE INCLINATION METHODS

101

- 3.5** Derive Eqs. (3.29) and (3.30) for the Newtonian pressure coefficient on an axisymmetric body including centrifugal effects.
- 3.6** The curves shown in Fig. 3.7 are changed when skin friction on the flat plate is included. In particular, the variation of L/D with α will peak at a low angle of attack and go to zero at $\alpha = 0$. (Why?) Let the drag coefficient caused by skin friction be assumed constant and denoted by C_{D_0} . Assuming a Newtonian pressure distribution, show that the maximum value of L/D is $0.667/C_{D_0}^{1/3}$ and occurs at an angle of attack (in radians) of $\alpha = C_{D_0}^{1/3}$. Furthermore, at $(L/D)_{\max}$ show that $C_{D_0} = \frac{1}{3}C_D$, where C_D is the total drag coefficient. [In other words, we can state that, at $(L/D)_{\max}$, wave drag is twice the friction drag.]
- 3.7** Using Newtonian theory, show that, at hypersonic speeds, stagnation pressure is about twice the dynamic pressure q_∞ , where, by definition, $q_\infty = \frac{1}{2}\rho_\infty V_\infty^2$.